5

Planetary boundary layer and turbulence parameterizations

5.1 Introduction

We have seen how the various properties of the land surface can influence the fluxes of energy that occur in the atmospheric surface layer. Now that these boundary conditions have been described, the next step is to determine how these energy fluxes influence the evolution of the atmosphere. This influence first occurs within the planetary boundary layer (PBL).

The planetary boundary layer is that part of the troposphere which is influenced directly by the presence of the Earth's surface, and responds to surface forcing with a timescale of an hour or less (Stull 1988). Thus, the land surface and the boundary layer are intimately tied together. The PBL can be as shallow as a few tens of meters, and as deep as several kilometers (Fig. 5.1). We previously learned in Chapters 2 and 3 that the values of temperature and specific humidity within the surface layer have a profound effect on the surface sensible and latent heat fluxes, since they are used in determining the potential difference between the soil–vegetation–land surface and the atmosphere. Now it is seen that the boundary layer responds to these fluxes over very short time periods. It also is important to recognize that turbulence, the irregular fluctuations that occur in fluid motions, is the dominant mechanism by which surface forcing is transmitted throughout the boundary layer.

One could arbitrarily say that the evolution of the boundary layer begins with sunrise. Just before sunrise the boundary layer is stable, as indicated by the potential temperature increasing with height (line "3" in Fig. 5.2). At sunrise, the radiant energy reaches the Earth's surface and begins to warm the ground (line "9"). Heat and moisture fluxes from the ground to the atmosphere become larger. The boundary layer responds to these fluxes by slowly deepening as thermals (bubbles of buoyant air that originate at the surface and rise into the boundary layer) reach the top of the boundary layer and

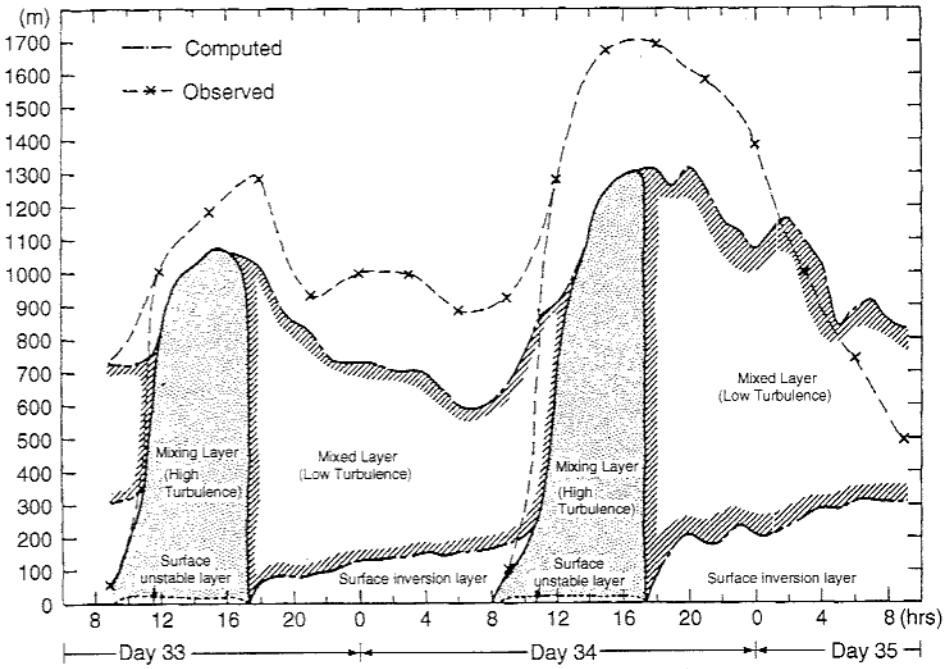

Figure 5.1. Schematic of the boundary layer evolution during days 33–35 from the Wangara experiment. During the daytime the mixing layer grows to depths above 1 km and is characterized by high levels of turbulence and a shallow and unstable surface layer. As the sun sets, the level of turbulence drops precipitously, leaving a residual layer behind. The surface inversion layer grows throughout the nighttime hours, influenced by episodic turbulence and radiational cooling. From Yamada and Mellor (1975).

overshoot their level of neutral buoyancy. Vertical velocities within thermals can reach 5 m s^{-1}, although values of 1–2 m s^{-1} are more common (Stull 1988). While thermals come in all shapes and sizes, the largest thermals typically have a horizontal length of ~1.5 times the boundary layer depth and are present over slightly less than half the boundary layer at any given time (Young 1988). Thermals are smaller early in the day, when the boundary layer is shallow, and become larger as the boundary layer deepens.

By the middle of the day, the boundary layer typically is near its maximum depth and often approaches a well-mixed structure (line "12" in Figs. 5.2 and 5.3). This occurs when turbulence is vigorous and it tends to uniformly mix the boundary layer, especially the potential temperature. Below the mixed layer is the surface layer, in which the potential temperature increases towards the warmer ground surface.

Above the mixed layer is the interfacial layer or inversion layer, in which the potential temperature increases with height. This layer separates the turbulent

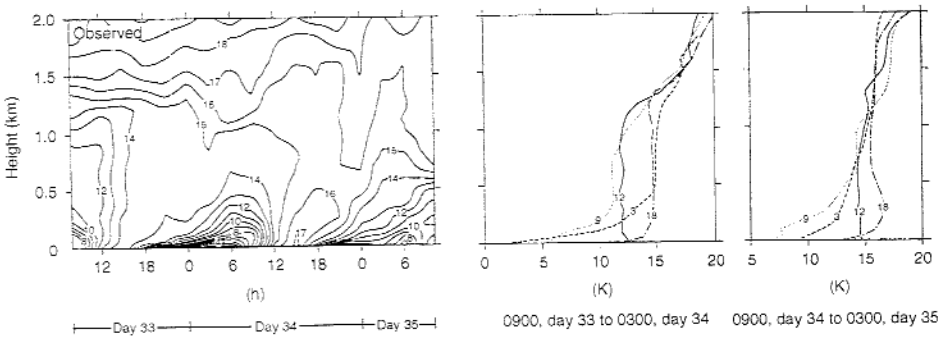

Figure 5.2. Observed boundary layer virtual potential temperature (θ_v) and vertical and temporal variations taken during the Wangara experiment over Hays, Australia. Isolines on the left-hand plot are $\theta_v - 273$ and shown in units of kelvin. Times indicated on the right-hand plots are local. From Yamada and Mellor (1975).

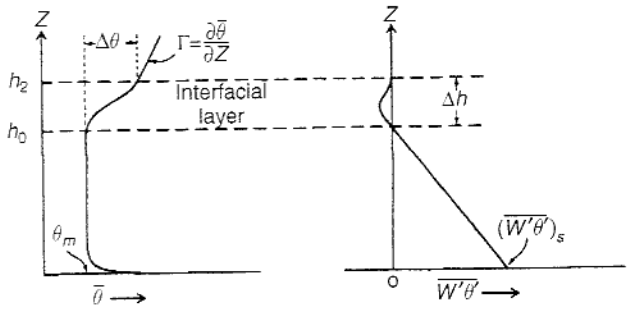

Figure 5.3. Illustration of a well-mixed boundary layer. The potential temperature is nearly constant with height within the mixed layer, and increases both below and above it. The heat flux profile is linear, with the largest value just above the ground and decreasing to zero at the top of the interfacial or inversion layer. From Deardorff (1979).

boundary layer from the less turbulent free atmosphere. The inversion layer is where entrainment occurs, the process by which the rising thermals overshoot their level of neutral buoyancy, owing to their upward momentum, and then sink back into the boundary layer bringing wisps or curtains of air from above the boundary layer into the boundary layer. Because of the vigorous turbulence in the boundary layer, the buoyant air from above is quickly mixed and becomes part of the boundary layer.

Since potential temperature increases with height, entrainment and surface sensible heat flux both act to increase the potential temperature of the boundary layer and help support the well-mixed structure of the boundary layer. However, moisture and momentum are not necessarily well mixed within the boundary

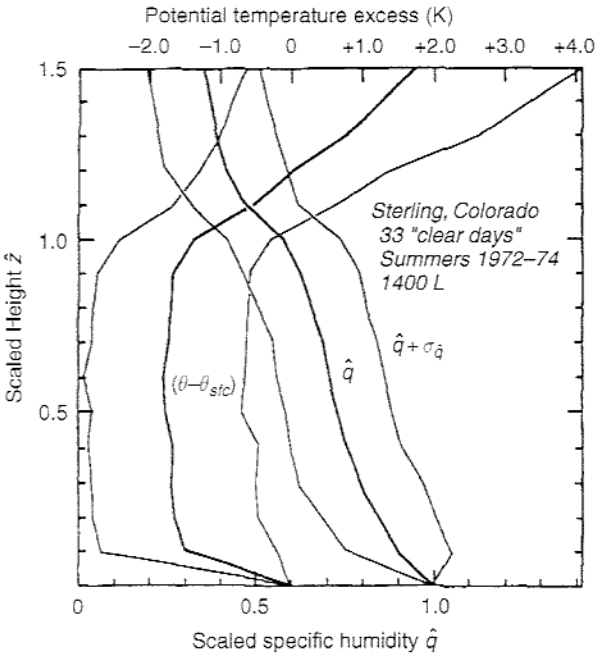

Figure 5.4. Vertical profiles of potential temperature (θ) and specific humidity (q), scaled by the surface value, at 1400 local time from Sterling, Colorado, averaged over 33 cloud-free days. Thin lines are the standard deviations, while θ_{sfc} is the surface value of potential temperature. Note that while the potential temperature is nearly constant with height below the boundary layer top near 1 km, the specific humidity clearly decreases with height in this same layer. From Mahrt (1976).

layer (Fig. 5.4). Since the free atmosphere above the boundary layer typically is drier than the boundary layer, moisture in particular often tends to decrease with height in the boundary layer. Indeed, Mahrt (1991) characterizes boundary layers into moistening and entrainment drying regimes, with moistening regimes occurring under large surface evaporation and large mean wind shear. Entrainment drying regimes are most often associated with small surface evaporation and unstable conditions. The diurnal evolution of the boundary layer often begins with a moistening regime in the morning, transitioning to an entrainment-drying regime later in the day. The boundary layer momentum field is even more complicated. Momentum may be well mixed within the boundary layer, particularly under quiescent synoptic-scale conditions, but momentum is strongly influenced by the larger-scale pressure gradients and often does not appear well mixed.

The daytime convective boundary layer is a complex phenomenon (Fig. 5.5). It is governed by turbulent processes, but also can be filled with more organized secondary features that interact with the turbulence (Brown

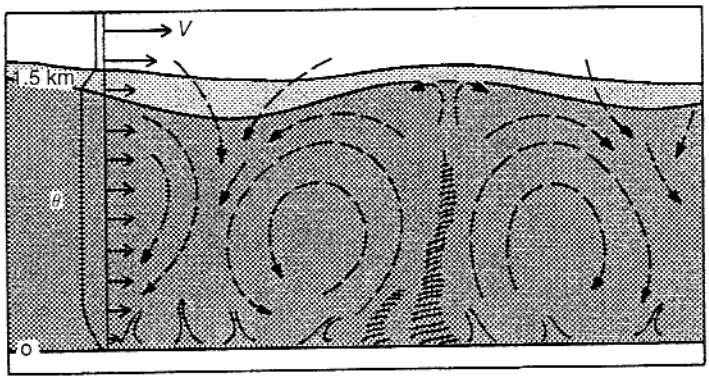

Figure 5.5. An artistic rendering of the daytime convective boundary layer, in which turbulence and organized thermals interact to vertically mix the layer. Note the entrainment of air from the free atmosphere into the boundary layer, and the horizontal changes in boundary layer depth. From Wyngaard (1985).

1980). These secondary features often take the form of boundary layer rolls, which act to help transfer the heat flux more efficiently (Stull 1988). Rolls are most often observed via satellite as cold air moves over a warm surface and creates lines of clouds (cloud streets), although clear air radar data indicate that roll-like circulations are a regular part of the boundary layer in the summertime when surface heating is strong. And, of course, rolls and other secondary circulations can occur at night just as well as the day, and occur throughout the year. During winter, boundary layer rolls are even thought to produce snowfall from time to time (Schultz *et al.* 2004).

So far this discussion makes it sound as though boundary layer evolution is governed only by the sensible heat flux from the ground surface. However, while buoyancy often is a main driver of daytime convective boundary layers, wind shear also generates turbulence and definitely plays a large role in boundary layer development. Schneider and Lilly (1999) investigate the daytime PBL just to the east of the Rocky Mountains and find that a combination of buoyancy and shear-produced turbulence controls the PBL evolution. The turbulent transfers in the upper portion of this PBL are tied to a complex field of interwoven vortical structures (Fig. 5.6) that are episodic and shift in response to local shear and buoyancy profiles. They conclude that a number of the common simplifying assumptions and scalings used for the boundary layer are inappropriate when describing this complex behavior. It is clear from their results that the boundary layer is not a simple system.

When clouds do not occur in the PBL, the boundary layer typically is fully turbulent throughout its depth during most of the daytime hours. When clouds

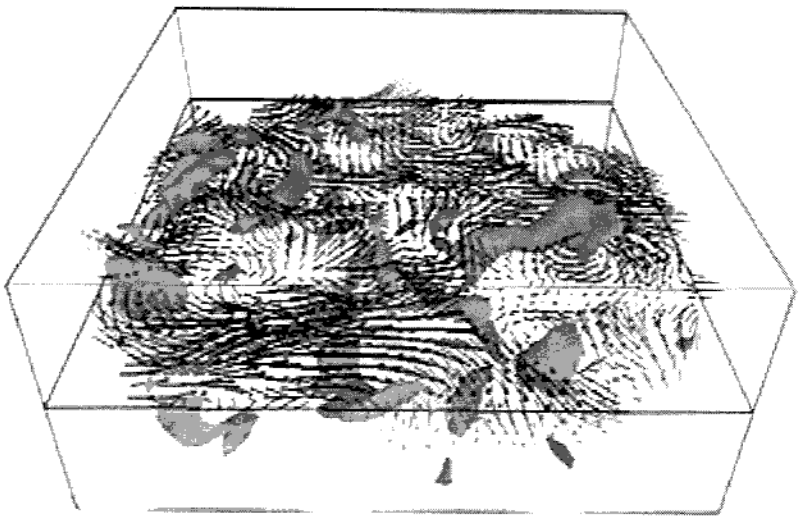

Figure 5.6. Visualization of wind vectors and isosurfaces of vorticity from 22 June 1984 during the Phoenix II experiment as derived from radar data. The reader is looking down on the analysis area and towards the north. The vorticity isosurfaces of $15 \times 10^{-3} s^{-1}$ show many vortical tubes within the turbulent flow, and these grow and decay over time. From Schneider and Lilly (1999).

are present the turbulence can be modified by the cloud circulations and sometimes the turbulence in the cloud becomes decoupled from the turbulence in the boundary layer below the cloud, especially when clouds completely cover the sky. Observations indicate that turbulence is an intrinsic part of the PBL and the largest eddies give a turbulent flow its distinguishing characteristics (Wyngaard 1985), so the effects of turbulence must be included in any attempt to understand and/or model the PBL. The lack of a complete understanding of a physical process, such as turbulence, does not mean that it cannot be modeled with some degree of confidence. One just needs to recognize the limitations of the models that are produced and selected for use.

As perhaps suggested by the results from Schneider and Lilly (1999), the nocturnal boundary layer, lacking the controlling influence of a strong surface buoyancy flux, is quite complex (Fig. 5.7). As the sun sets, the heat fluxes from the surface are reduced and the air near the ground surface begins to cool as radiational cooling dominates the surface energy budget. Potential temperature again increases with height, and wind shear is the main source for generating turbulence. Thus, turbulence in the nocturnal PBL is often intermittent. The air above the surface inversion layer is the residual from the daytime convective boundary layer. In addition, drainage flows occur very near the surface owing to variations in elevation, and gravity waves may

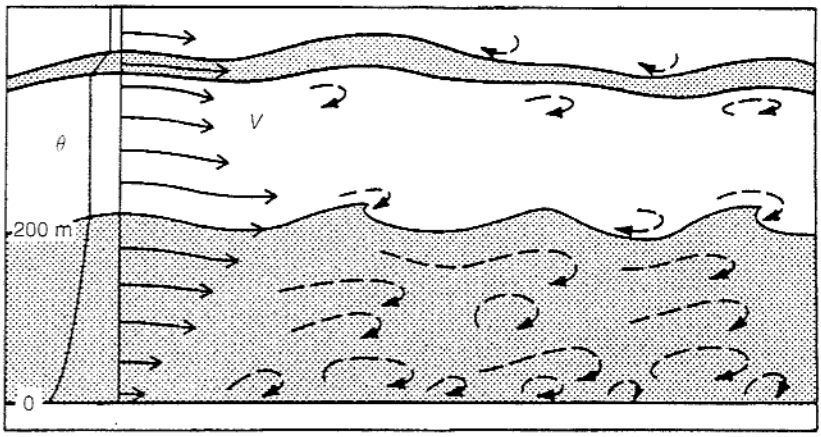

Figure 5.7. An artistic rendering of the nocturnal boundary layer, in which turbulence is generated by the mean vertical wind shear and gravity waves are superimposed upon the flow. Note the presence of a nocturnal wind jet at the top of the thin turbulent layer. From Wyngaard (1985).

develop within the stable boundary layer and further complicate the flow. Wyngaard (1985) nicely outlines the delicate and precarious balance between turbulence generated by the mean wind shear and its dissipation from viscous effects and buoyancy.

The nocturnal boundary layer also is well-known as a breeding ground for low-level jets. A low-level jet is a wind speed maximum that occurs in the lowest few kilometers of the atmosphere. These jets are observed worldwide, are important to the horizontal and vertical fluxes of temperature and moisture, and often are associated with the development and evolution of deep convection (Stensrud 1996). While low-level jets are observed during the daytime and can be caused by a number of different mechanisms (see Stensrud 1996), they are strongest and most commonly observed at night. One mechanism for producing low-level jets is a diurnal variation of eddy viscosity as discussed by Blackadar (1957). During the daytime, the boundary layer is strongly coupled to the surface layer and frictional effects cause the boundary layer winds to be subgeostrophic. When turbulent mixing ceases and a shallow nocturnal boundary layer begins to develop, the winds above the nocturnal inversion are decoupled from the surface layer and are no longer in balance. This imbalance between the Coriolis and pressure gradient forces induces an inertial oscillation of the wind that produces a wind speed maximum approximately 6–8 h after turbulent mixing ceases (see Hoxit 1975). Low-level jets are not only important to weather and climate, but also are used by birds and insects to assist in their migrations (Drake 1985).

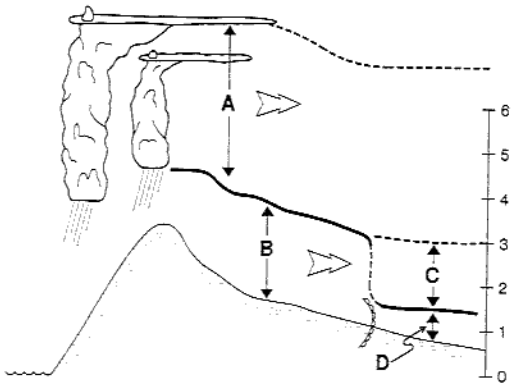

Figure 5.8. Depiction of two vastly different elevated residual layers being created, with the environmental wind blowing from left to right. Layer B is dry adiabatic, well mixed, and has low relative humidity. This layer is advected over layer D, forming an elevated residual layer (C). Layer D in this case is a moist boundary layer. Layer A, assuming that the convection is widespread and long-lived, is moist adiabatic and has high relative humidity. Thus, the airmass over layer D has a three-layer structure that is defined by boundary layer processes (active or past) over much of its depth. From Stensrud (1993).

The contrast between daytime and nighttime PBLs is dramatic, yet both must be represented within boundary layer schemes. Owing to the complexity of the boundary layer, the parameterization schemes used in operational forecast models and even most research models are focused upon representing the evolution of the mean boundary layer state through the diurnal cycle and include the effects of turbulence indirectly.

The evolution of boundary layers is important not only because these layers largely determine the characteristics of the conditions we live in each day (how hot or dry, and how windy it will be), but also because boundary layers over elevated terrain can be advected over regions with lower terrain, and thereby influence the development of other boundary layers (Fig. 5.8). This process is a frequent occurrence over central USA (Carlson *et al.* 1983; Lanicci and Warner 1991), and likely anywhere else downwind of mountain ranges. These boundary layers that are advected off elevated terrain are called elevated mixed layers or elevated residual layers, since their potential temperature profiles are often well mixed. These layers have a large effect on the convective available potential energy and often are seen within the environments of severe weather. This only further emphasizes the importance of parameterizing boundary layers correctly.

The evolution of the boundary layer often sets limits on the types of atmospheric phenomena that can be produced on a given day. Boundary layers that

are shallow and moist may produce thermals that are too small to reach their level of free convection and produce deep convection. However, under the same conditions, boundary layers that are too deep may become too dry from entrainment and thereby remove any possibility of deep convection. Thus, another reason why boundary layers are important to weather prediction is that the potential for deep convection is closely tied to the boundary layer structure. It is well-known that deep convection strongly influences numerical weather prediction from very short-range forecasts to climate predictions.

While the equations of motion can be applied directly to turbulent flows, the models most appropriate for this application would need an exceedingly small grid spacing (of the order of 50 m or less), and there would still be eddies that would not be represented on the model grid. The effects of these subgrid eddies still need to be accounted for in some way, which usually is based upon a statistical approach to the eddy effects. A useful technique called Reynolds averaging is now outlined that sets the mathematical stage for looking at how turbulent flows influence boundary layer development.

5.2 Reynolds averaging

We begin the study of turbulent effects with the basic equations of motion and statistically average over the smaller eddy sizes. Each dependent variable in the equations of motion is assumed to be represented by a mean and a perturbation from the mean as defined by $A = \bar{A} + a'$. For example, assume there are two variables A and B, both defined as a mean quantity plus a perturbation. When they are multiplied together, what happens when they are averaged over some time period? The result is

$$\overline{A \cdot B} = \overline{(\bar{A} + a')(\bar{B} + b')} = \overline{\bar{A}\bar{B} + \bar{A}b' + \bar{B}a' + a'b'} = \bar{A}\bar{B} + \overline{a'b'}, \qquad (5.1)$$

since the perturbation terms a' and b', even when multiplied by a constant such as $\bar{A}$, average to zero over the given time period by definition. However, when the perturbation terms are multiplied together, the end result is not necessarily zero. The last term on the right represents the influence of the eddy motions. Thus, even though the evolution of the mean quantities is of primary interest, the eddies clearly play a significant role in determining how these mean quantities change. The process of separating a given variable into a mean and a perturbation component, and then averaging over time, is called Reynolds averaging.

When dealing with the full equations of motion, instead of this simple two-variable example of Reynolds averaging, using summation notation to write

the equations is very helpful in simplifying the derivations. Summation notation is a compact way to represent several different equations in one. Define

x_i as a generic distance, with $x_1 = x, x_2 = y, x_3 = z$

u_i as a vector, with $u_1 = u, u_2 = v, u_3 = w$

δ_i as a unit vector, with $\delta_1 = \vec{i}, \delta_2 = \vec{j}, \delta_3 = \vec{k}$

and

δ_{mn} as the Kronecker delta which equals 1 when $m = n$ and zero otherwise.

The alternating unit tensor is defined as

$$\varepsilon_{ijk} = \begin{cases} +1, & \text{if } i,j,k \text{ are in ascending order} \\ -1, & \text{if } i,j,k \text{ are in descending order} \\ 0, & \text{otherwise,} \end{cases}$$

where an ascending order means that the values of *ijk* are in a sequence of 1, 2, 3, or 2, 3, 1, or 3, 1, 2. Descending order is the opposite, such as 3, 2, 1, or 2, 1, 3, or 1, 3, 2. The alternating unit tensor is zero if any of the values of *ijk* are the same.

The summation notation also requires the application of two basic rules. The first rule is that one sums on repeated indices when they appear in two quantities that are multiplied together. The second rule is that all indices take on the values of 1, 2, and 3. For example, a single term in summation notation such as

$$u_i \frac{\partial \theta}{\partial x_i} = u_1 \frac{\partial \theta}{\partial x_1} + u_2 \frac{\partial \theta}{\partial x_2} + u_3 \frac{\partial \theta}{\partial x_3} = u \frac{\partial \theta}{\partial x} + v \frac{\partial \theta}{\partial y} + w \frac{\partial \theta}{\partial z}, \tag{5.2}$$

which allows us to combine a number of separate terms and even equations into a very compact format.

5.3 Turbulence closure

To explore the role of turbulence in the evolution of the planetary boundary layer, the Boussinesq equations of motion are used (Dutton and Fichtl, 1969). The momentum equations are written in summation notation as

$$\frac{\partial u_i}{\partial t} + u_j \frac{\partial u_i}{\partial x_j} = -\delta_{i3}\left(g - \frac{\theta_v'}{\overline{\theta}_v} g\right) + f\varepsilon_{ij3}u_j - \frac{1}{\overline{\rho}} \frac{\partial p}{\partial x_i} + \nu \frac{\partial^2 u_i}{\partial x_j^2}. \tag{5.3}$$

The next step is to expand each variable into a mean and a perturbation, where the perturbations are assumed to represent the effects of eddies, or turbulence, yielding

$$\frac{\partial(\bar{u}_i + u_i')}{\partial t} + \frac{(\bar{u}_j + u_j')\partial(\bar{u}_i + u_i')}{\partial x_j}$$
$$= -\delta_{i3}\left(g - \frac{\theta_v'}{\bar{\theta}_v}g\right) + f\varepsilon_{ij3}(\bar{u}_j + u_j') - \frac{1}{\bar{\rho}}\frac{\partial(\bar{p} + p')}{\partial x_i} + \nu\frac{\partial^2(\bar{u}_i + u_i')}{\partial x_j^2}. \quad (5.4)$$

Now all the terms are multiplied out and separated to obtain

$$\frac{\partial \bar{u}_i}{\partial t} + \frac{\partial u_i'}{\partial t} + \bar{u}_j\frac{\partial \bar{u}_i}{\partial x_j} + \bar{u}_j\frac{\partial u_i'}{\partial x_j} + u_j'\frac{\partial \bar{u}_i}{\partial x_j} + u_j'\frac{\partial u_i'}{\partial x_j}$$
$$= -\delta_{i3}\left(g - \frac{\theta_v'}{\bar{\theta}_v}g\right) + f\varepsilon_{ij3}\bar{u}_j + f\varepsilon_{ij3}u_j' - \frac{1}{\bar{\rho}}\frac{\partial \bar{p}}{\partial x_i} - \frac{1}{\bar{\rho}}\frac{\partial p'}{\partial x_i} + \nu\frac{\partial^2 \bar{u}_i}{\partial x_j^2} + \nu\frac{\partial^2 u_i'}{\partial x_j^2}. \quad (5.5)$$

This equation represents the evolution of both the mean and the turbulent portions of the momentum equation. But only the evolution of the mean portion is of interest, which is what the models predict, so we average over the entire equation. This yields

$$\frac{\partial \bar{u}_i}{\partial t} + \bar{u}_j\frac{\partial \bar{u}_i}{\partial x_j} + \overline{u_j'\frac{\partial u_i'}{\partial x_j}} = -\delta_{i3}g + f\varepsilon_{ij3}\bar{u}_j - \frac{1}{\bar{\rho}}\frac{\partial \bar{p}}{\partial x_i} + \nu\frac{\partial^2 \bar{u}_i}{\partial x_j^2}. \quad (5.6)$$

How does this equation differ from the original Boussinesq equation for momentum? There are two changes apparent. One is that the term with the perturbation virtual potential temperature, which represented the effects of buoyancy, has disappeared. The second change is that a new term, $\overline{u_j'(\partial u_i'/\partial x_j)}$, has been added. This new term represents the advection of turbulence by turbulence.

It would be helpful to write the turbulence advection term in a more useful form. If the atmosphere is assumed to be incompressible in the boundary layer, i.e. assume that the shallow Boussinesq approximation is valid (which for the boundary layer is a pretty good assumption), then

$$\frac{\partial u_j}{\partial x_j} = 0 \quad \text{or} \quad \frac{\partial \bar{u}_j}{\partial x_j} + \frac{\partial u_j'}{\partial x_j} = 0. \quad (5.7)$$

If we again average over time, this results in

$$\frac{\partial \bar{u}_j}{\partial x_j} = 0, \quad (5.8)$$

and since

$$\frac{\partial \bar{u}_j}{\partial x_j} + \frac{\partial u'_j}{\partial x_j} = 0, \tag{5.9}$$

then (5.8) and (5.9) require that

$$\frac{\partial u'_j}{\partial x_j} = 0. \tag{5.10}$$

Thus, both the mean wind and the perturbation wind components are incompressible. If the divergence of the perturbation wind is multiplied by any quantity, even a perturbation, then it is still zero since it must always be zero. From this knowledge, it is apparent that

$$\overline{\frac{\partial (u'_i u'_j)}{\partial x_j}} = \overline{\frac{u'_i \partial u'_j}{\partial x_j}} + \overline{\frac{u'_j \partial u'_i}{\partial x_j}} = \overline{\frac{u'_j \partial u'_i}{\partial x_j}}. \tag{5.11}$$

Using this result to rearrange the terms in the equation for the time rate of change of the mean momentum, after Reynolds averaging, gives

$$\frac{\partial \bar{u}_i}{\partial t} + \bar{u}_j \frac{\partial \bar{u}_i}{\partial x_j} = -\delta_{i3} g + f \varepsilon_{ij3} \bar{u}_j - \frac{1}{\bar{\rho}} \frac{\partial \bar{p}}{\partial x_i} + \nu \frac{\partial^2 \bar{u}_i}{\partial x_j^2} - \frac{\partial \overline{(u'_i u'_j)}}{\partial x_j}. \tag{5.12}$$

The last term on the right-hand side of this equation is called the Reynolds stress (covariance) term. Now, numerical models predict the mean variables, but what about this Reynolds stress term? Since it is not predicted explicitly, there are two options. First, an empirical relationship can be derived between this term and known model variables (parameterize). Second, additional equations can be derived to predict the Reynolds stress term explicitly.

Recall that we began with the Boussinesq equation for momentum, and then divided each variable into a mean and a perturbation component. If we now begin with the equation that represents the evolution of both the mean and turbulent portions of the momentum equation, then we can subtract off (5.6) for the mean and the result is an equation for the time rate of change of a turbulent gust. This process yields

$$\frac{\partial u'_i}{\partial t} + \bar{u}_j \frac{\partial u'_i}{\partial x_j} + u'_j \frac{\partial \bar{u}_i}{\partial x_j} + u'_j \frac{\partial u'_i}{\partial x_j} = \delta_{i3} \left(\frac{\theta'_v}{\bar{\theta}_v} g \right) + f \varepsilon_{ij3} u'_j - \frac{1}{\bar{\rho}} \frac{\partial p'}{\partial x_i} + \nu \frac{\partial^2 u'_i}{\partial x_j^2} + \frac{\partial \overline{(u'_i u'_j)}}{\partial x_j}. \tag{5.13}$$

To develop additional equations to predict the Reynolds stress term explicitly, an equation for the time rate of change of $\overline{u'_i u'_j}$ is needed. Therefore, using the equation for the turbulent gust, and noting that one can change j to k in the

equation since when using summation notation all indices take on the values 1, 2, and 3, it is found that

$$\frac{\partial\overline{(u_i'u_k')}}{\partial t} = \overline{u_i'\frac{\partial u_k'}{\partial t}} + \overline{u_k'\frac{\partial u_i'}{\partial t}}. \tag{5.14}$$

So to obtain the evolution of the Reynolds stress term, simply multiply the equation for the turbulent gust by u_k' to produce the second term on the right-hand side of the above equation. The first term on the right-hand side can be determined by taking the equation for the turbulent gust, changing all the i-indices to k-indices and then multiplying by u_i'. The end result is

$$\begin{aligned}\frac{\partial\overline{(u_i'u_k')}}{\partial t} + \bar{u}_j\frac{\partial\overline{(u_i'u_k')}}{\partial x_j} = &-\overline{(u_i'u_j')}\frac{\partial\bar{u}_k}{\partial x_j} - \overline{(u_k'u_j')}\frac{\partial\bar{u}_i}{\partial x_j} - \frac{\partial\overline{(u_i'u_j'u_k')}}{\partial x_j}\\ &+\frac{g}{\bar{\theta}_v}\left(\delta_{k3}\overline{u_i'\theta_v'} + \delta_{i3}\overline{u_k'\theta_v'}\right) + f\left(\varepsilon_{kj3}\overline{u_i'u_j'} + \varepsilon_{ij3}\overline{u_k'u_j'}\right)\\ &-\frac{1}{\bar{\rho}}\left[\frac{\partial\overline{(p'u_k')}}{\partial x_i} + \frac{\partial\overline{(p'u_i')}}{\partial x_k} - \overline{p'\left(\frac{\partial u_i'}{\partial x_k} + \frac{\partial u_k'}{\partial x_i}\right)}\right]\\ &+\nu\frac{\partial^2\overline{(u_i'u_k')}}{\partial x_j^2} - 2\nu\overline{\frac{\partial u_i'}{\partial x_j^2}\frac{\partial u_k'}{\partial x_j}}.\end{aligned} \tag{5.15}$$

This represents nine different equations, including equations for $\overline{u'u'}, \overline{u'v'}, \overline{u'w'}, \overline{v'v'}, \overline{v'w'}$, and $\overline{w'w'}$. However, the total number of equations is reduced to six owing to symmetry (e.g., $\overline{u'v'} = \overline{v'u'}$).

Equations for the mean momentum variables and for the Reynolds stress terms are now available, so they can be included in a numerical model and integrated forward in time. However, closer inspection reveals that yet another unknown term is present in the equation for the Reynolds stress, namely the $\partial\overline{(u_i'u_j'u_k')}/\partial x_j$ term. This unknown is now a triple correlation term! As this pattern suggests, if equations for the triple correlation term are developed, then a quadruple correlation term is created. This cascading of unknowns is called the *turbulence closure* problem. There are always more unknowns than equations, so at some point the remaining unknown terms need to be parameterized by relating them to some combination of the known variables. Stull (1988) shows the turbulence closure problem that occurs in the remaining equations of motion.

There are two related terms that describe where in this cascade of unknowns assumptions are made, and define the most complex correlation terms that are related to known variables. These terms are "order" and "level". Both terms are found in the meteorology literature, but the term order is used here. First-order

closure means that there are equations for the state variables (u, v, w, T, q), or the first moments, and the covariance terms (e.g., $\overline{u'v'}$) are parameterized. Second-order closure means that there are equations for both the state variables and the covariance terms, and the triple correlation terms are parameterized. There also are examples of non-integer closures, such as half-order and one-and-a-half-order closure. Part of the motivation for higher-order closures is that, for example, "if a crude assumption for second moments predicts first moments adequately, perhaps a crude assumption for third moments will predict second moments adequately" (Lumley and Khajeh-Nouri[1] 1974, p. 171).

When the unknown terms in the equations are related to the known variables, there are two very different approaches that can be used for boundary layer parameterization. One approach is called *local closure*, and the other approach is called *non-local closure*. Local closure relates the unknown variables to known variables at nearby vertical grid points. Thus, when the model is solving for the Reynolds stress term at $z = 500$ m, only the model variables within a small distance around $z = 500$ m are used for the unknown terms. In contrast, non-local closure relates the unknown variables to known variables at any number of other vertical grid points. So for the same situation, a non-local closure scheme may use all the vertical grid points within the boundary layer to determine the unknown terms and to solve for the Reynolds stress term at $z = 500$ m. As can be seen, these approaches are conceptually very different and can result in dramatically different evolutions of the boundary layer. Some common closure approaches are now explored.

5.4 Non-local closure schemes

The boundary layer is influenced directly by what is happening at the Earth's surface and responds to changes in surface forcing very quickly. Most of the turbulent energy is found in the largest eddies, which typically are of the depth of the boundary layer. The potential benefits of a non-local interpretation are illustrated in Stull (1991), where he clearly shows that a non-local viewpoint explains the turbulent characteristics of a boundary layer above a forest canopy, whereas a local viewpoint produces expectations that do not match observations of the heat flux (Fig. 5.9). It is clear that non-local approaches have a number of advantages over local approaches, and so we begin with the simplest non-local approach – a mixed layer scheme. We then move toward more sophisticated schemes that are representative of the non-local schemes most commonly used in atmospheric models.

[1] Reprinted with permission from Elsevier.

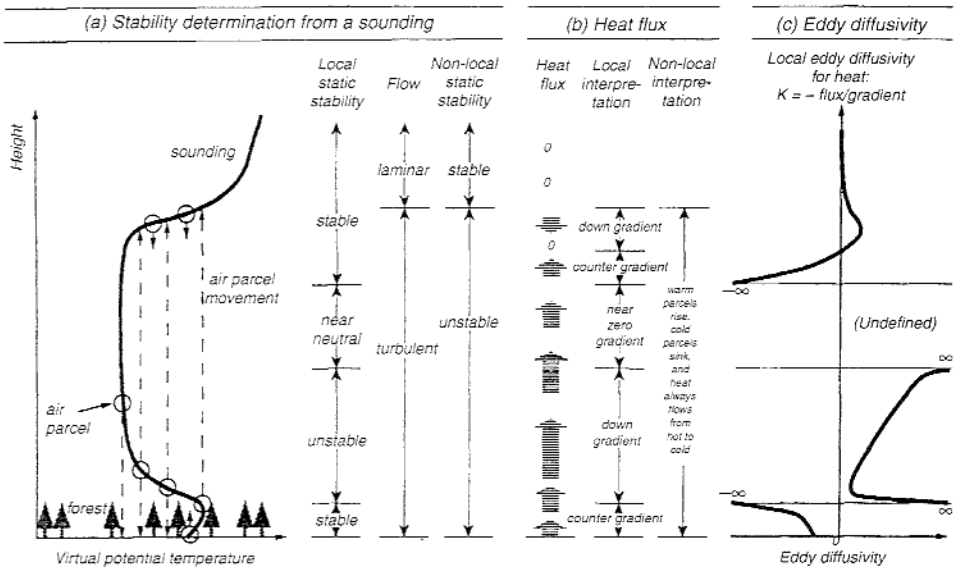

Figure 5.9. Local versus non-local interpretations of boundary layer stability and associated turbulence. A typical sounding from above a forest canopy is shown in (a), illustrating the local static stability and turbulent conditions. The heat flux is shown in (b), with the local and non-local interpretations of this flux. The calculated eddy diffusivity is shown in (c), further illustrating the challenges to local interpretations of this boundary layer that lead to incorrect expectations for turbulence. From Stull (1991).

5.4.1 Mixed layer schemes

Mixed layer models were first developed in the 1960s and were used to explore stratocumulus development by Lilly (1968) and later for general boundary layer development (Carson 1973; Betts 1973). Mixed layer models are still used in many ocean models, and are quite efficient computationally.

The basic assumptions in mixed layer models are that potential temperature is constant with height in the mixed layer, and that the mixed layer is horizontally homogeneous. Neglecting the effects of horizontal advection, one finds that

$$\frac{\partial \overline{\theta}}{\partial t} = -\frac{\partial}{\partial z}\left(\overline{w'\theta'}\right). \tag{5.16}$$

for a mixed layer model. Since the potential temperature is constant with height, $\overline{w'\theta'}$ must vary linearly with height (as often observed) and, therefore, the only fluxes that are important to the change of potential temperature with time occur at the top and bottom boundaries. This leads to

$$\frac{\partial \bar{\theta}}{\partial t} = \left[\left(\overline{w'\theta'} \right)_S - \left(\overline{w'\theta'} \right)_H \right] \left(\frac{1}{H} \right). \tag{5.17}$$

where H is the top height of the mixed layer and the subscript S represents fluxes from the ground surface.

The surface fluxes are obtained from calculations of Q_H as discussed in Chapters 2 and 3, so all that is needed is an equation for the fluxes at the top of the boundary layer. The flux at the top of the mixed layer is equal to the turbulent entrainment of potential temperature into the mixed layer as the mixed layer grows and ingests parcels of air from above. Assuming no change in the mixed layer depth due to environmental subsidence or lifting, this can be described mathematically as

$$\left(\overline{w'\theta'} \right)_H = -\frac{dH}{dt} \left(\theta_- - \bar{\theta} \right). \tag{5.18}$$

where θ_- is the potential temperature of the air just above the mixed layer top as shown in Fig. 5.10.

This result can be derived using Liebniz' rule for differentiation of integrals (Dutton 1976). Recall that this rule states that

$$\frac{d}{dt} \int_a^b F(x,t)\, dx = \int_a^b \frac{\partial F(x,t)}{\partial t}\, dx + F(b,t) \frac{db}{dt} - F(a,t) \frac{da}{dt}. \tag{5.19}$$

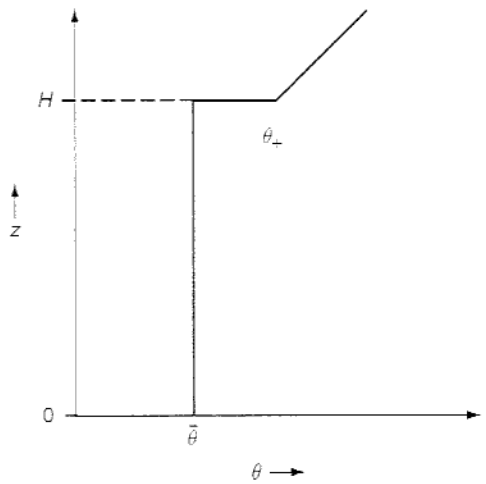

Figure 5.10. Illustration of a mixed-layer model profile of potential temperature (θ) versus height (z) in which the potential temperature is constant within the mixed layer and there is a discontinuity of potential temperature at the top of the layer (H). The value θ_- defines the potential temperature at the bottom of the atmospheric layer that lies on top of the mixed layer.

By assuming that $F(x, t) = \theta(z, t)$ and integrating across the inversion layer it is found that

$$\int_{H_-}^{H_+} \frac{\partial \theta}{\partial t}\, dz = \frac{d}{dt}\int_{H_-}^{H_+} \theta\, dz - \theta_+ \frac{dH_+}{dt} + \bar{\theta}\frac{dH_-}{dt}, \tag{5.20}$$

where H_+ is a height level just above the inversion height H, and H_- is a height level just below the inversion height H. Also note that the terms are reordered slightly to move the partial derivative to the left-hand side of the equal sign. Recalling the definition of the time rate of change of the mixed layer potential temperature, namely

$$\frac{\partial \theta}{\partial t} = -\frac{\partial}{\partial z}\left(\overline{w'\theta'}\right), \tag{5.21}$$

and substituting this expression into the left-hand side term of Liebniz' rule in (5.20) yields

$$\int_{H_-}^{H_+} \frac{\partial \theta}{\partial t}\, dz = -\int_{H_-}^{H_+} \frac{\partial\left(\overline{w'\theta'}\right)}{\partial z}\, dz = \left(\overline{w'\theta'}\right)_H, \tag{5.22}$$

since by definition the flux is zero above the mixed layer at H_+. By the mean value theorem, there exists a mean value of θ, say $\tilde{\theta}$, for which $\bar{\theta} < \tilde{\theta} < \theta_+$, allowing the first term on the right-hand side of Liebniz' rule in (5.20) to be rewritten as

$$\frac{d}{dt}\int_{H_-}^{H_+} \theta\, dz = \frac{d}{dt}\left[\tilde{\theta}(H_+ - H_-)\right], \tag{5.23}$$

which goes to zero as H_+ and H_- both approach H. Finally, as H_+ and H_- approach the same value H we obtain from (5.20) that

$$\left(\overline{w'\theta'}\right)_H = -\frac{dH}{dt}\left(\theta_+ - \bar{\theta}\right) = -\frac{dH}{dt}\Delta\theta. \tag{5.24}$$

This equation predicts the rise in mixed layer depth in the absence of environmental subsidence or lifting, but the system of equations is still not closed. One solution is that laboratory measurements (Deardorff *et al.* 1969) suggest

$$\left(\overline{w'\theta'}\right)_H = -0.2\left(\overline{w'\theta'}\right)_S = -k_e\left(\overline{w'\theta'}\right)_S, \tag{5.25}$$

where k_e is an entrainment coefficient. This relationship then closes the system of equations. As seen later, there is some uncertainty in the value

of k_e. Regardless, if the following expression is used for the surface sensible heat flux,

$$\left(\overline{w'\theta'}\right)_S = \frac{\left(\theta_S - \overline{\theta}\right)}{r_H}, \tag{5.26}$$

then a set of two equations is obtained that describes the evolution of the mixed layer

$$\frac{d\overline{\theta}}{dt} = \frac{(1+k_e)\left(\theta_S - \overline{\theta}\right)}{r_H H} = (1+k_e)\frac{Q_H}{\rho c_p H}, \tag{5.27}$$

$$\frac{dH}{dt} = \frac{k_e\left(\theta_S - \overline{\theta}\right)}{r_H \Delta\theta} = \frac{k_e Q_H}{\rho c_p \Delta\theta}. \tag{5.28}$$

When the surface skin temperature is held constant, as happens over short timescales when air moves over the oceans, the mixed layer temperature approaches the surface skin temperature (Fig. 5.11). However, the depth of the mixed layer is very much dependent upon the amount of entrainment.

One can also include mixed layer equations for moisture and momentum, such that

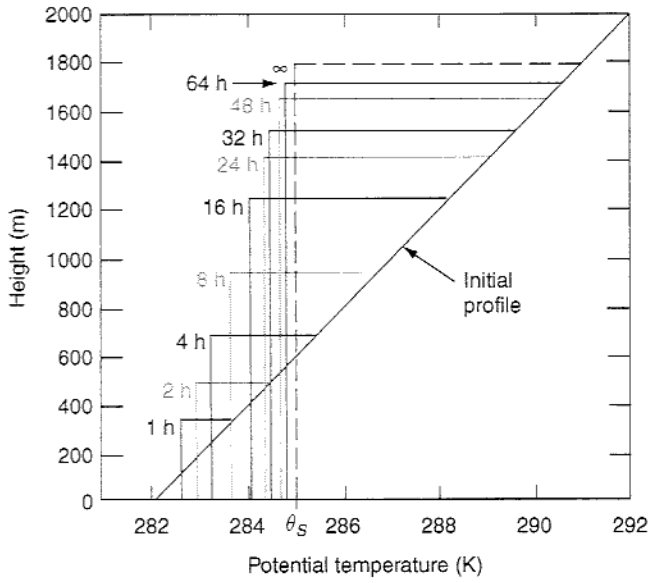

Figure 5.11. Evolution of the potential temperature versus height within a mixed layer model as a function of time. Note that as time becomes infinite, the mixed layer temperature and the surface skin temperature are equal. From Lilly (1968).

$$\frac{d\bar{q}}{dt} = \frac{1}{H}\left(\frac{Q_E}{\rho L_v} + \frac{k_e Q_H \Delta q}{\rho c_p \Delta\theta}\right), \tag{5.29}$$

$$\frac{d\vec{V}_H}{dt} = -f\vec{k} \times (\vec{V}_H - \vec{V}_g) + C_D \vec{V}_H \cdot \left(-\vec{V}_H + \frac{k_e Q_H \Delta \vec{V}_H}{\rho c_p \Delta\theta}\right)\frac{1}{H}, \tag{5.30}$$

where the H subscript on the wind vector denotes the horizontal wind, C_D is a dimensionless drag coefficient, Δ refers to differences across the top of the mixed layer for either specific humidity or momentum, f is the Coriolis force, and the g subscript denotes the geostrophic wind.

Artaz and Andre (1980) compare different mixed layer schemes and find that the ones that directly relate the inversion-level heat flux to the surface sensible heat flux perform as well as any of the other approaches in predicting mixed layer depth. However, the greatest uncertainty in these schemes is the value of the entrainment coefficient. For free convective conditions, values of 0.1–0.4 appear to be reasonable (Stull 1976; Heidt 1977). However, Dubosclard (1980) suggests an entrainment coefficient near 1.0 for situations when the surface sensible heat flux is small. Betts *et al.* (1992) argue that 0.4 is a better value than the traditional value of 0.2, while Margulis and Entekhabi (2004) calculate a range of values from 0.22 to 0.54 by coupling observations with a mixed layer model. It is clear that the range of values for the entrainment coefficient determined from observational data is large and that the value chosen has a significant effect on the resulting mixed layer evolution.

Mixed layer schemes are also used by Betts *et al.* (1990, 1992) as the foundation for examining boundary layer budgets. The approach outlined in these studies allows one to display graphically (in two-dimensional vector form) the mixed layer energy budget on a conserved variable diagram, with vectors representing the surface flux, the mixed layer tendency, and the entrainment flux (Fig. 5.12). The origin of all three vectors is determined directly from the observed values of the mixed layer mean potential temperature and the mixing ratio. The surface flux vector is determined from observations of the sensible and the latent heat flux, and indicates the warming and moistening that would occur in the mixed layer if surface fluxes alone determined mixed layer evolution. The mixed layer tendency vector is determined directly from the observed values of the mixed layer mean potential temperature and the mixing ratio at a later time. Finally, the direction of the entrainment flux vector is determined from rawinsonde observations as the sonde penetrates the inversion layer. The magnitude of the entrainment flux vector is calculated using the assumption that the surface and entrainment fluxes together determine the evolution of the mixed layer, such that the sum of

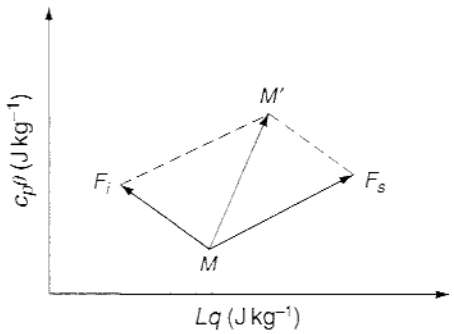

Figure 5.12. Vector diagrams for the mixed layer budget, with M representing the initial mixed layer, M' representing the mixed layer at a later time, F_s representing the surface flux vector, F_i representing the entrainment flux vector. After Betts (1992).

the surface flux and entrainment flux vectors equals the mixed layer tendency vector (Fig. 5.12). The entrainment coefficient can then be determined by projecting the vectors $\vec{F}_s$ and $\vec{F}_i$ onto a dry virtual adiabat (see Betts 1992). This technique provides a good conceptual picture of boundary layer evolution, and is another way in which mixed layer schemes continue to be valuable in meteorology. Mixed layer schemes have even been used to study cirrus outflow dynamics (Lilly 1988).

5.4.2 *Penetrative convection scheme*

Estoque (1968) visualizes the exchange of heat in the boundary layer as taking place between the ground surface and each level within the mixed layer, a clear example of a non-local viewpoint. This assumption leads to a heat flux distribution that depends upon the entire temperature distribution within the boundary layer, such that countergradient fluxes are a natural outcome of this approach. Blackadar (1978) develops a one-dimensional boundary layer model based upon this idea, as outlined and tested in Zhang and Anthes (1982). This scheme is often referred to as the Blackadar scheme.

Assume that the intensity of mixing under free convection depends upon the surface layer temperature (θ_{sl}) and the heat flux at the top of the surface layer ($Q_{H_{sl}}$). Priestley (1954) derives an expression for the heat flux at the top of the surface layer, in which

$$Q_{H_{sl}} = \rho c_p z_{sl} b(\theta_{sl} - \theta_{sl+\Delta z})^{3/2}, \tag{5.31}$$

where z_{sl} is the thickness of the surface layer, $\theta_{sl+\Delta z}$ is the potential temperature of the first model layer above the surface layer, ρ is the density, g is the acceleration due to gravity, and

$$b = \left(\frac{2g}{27\theta_{sl}}\right)^{1/2} \frac{1}{z_{sl}} \left[z_{sl}^{-1/3} - 2(z_{sl+\Delta z})^{-1/3}\right]^{-3/2}. \tag{5.32}$$

The time rate of change of the surface layer potential temperature is then

$$\frac{\partial \theta_{sl}}{\partial t} = \frac{(Q_H - Q_{H_{sl}})}{\rho c_p z_{sl}}, \tag{5.33}$$

which is simply proportional to the difference of the fluxes into and out of the surface layer. This is another example of how the depth of the atmospheric layers influences parameterization scheme behavior, as a thinner surface layer leads to a faster response in the surface layer potential temperature.

Within the convective boundary layer, the time rate of change of potential temperature is given by

$$\frac{\partial \theta(z)}{\partial t} = \overline{m} w(z)[\theta_{sl} - \theta(z)]. \tag{5.34}$$

Here $\overline{m}$ is the fraction of mass exchanged between the boundary layer and the free atmosphere above, and $w(z)$ is a weighting function used to account for variations in the exchange rate. Typically, $w(z) = 1$ at all heights, although Estoque (1968) proposed that $w(z)$ should decrease linearly as a function of boundary layer height.

To determine $\overline{m}$, it is assumed that no flux occurs across the top of the boundary layer, such that

$$Q_{H_{sl}} - \overline{m} \rho c_p \int_{z_{sl}}^{z_{top}} [\theta_{sl} - \theta(z)]\, dz = 0, \tag{5.35}$$

and therefore

$$\overline{m} = Q_{H_{sl}} \left[\rho c_p (1 - k_e) \int_{z_{sl}}^{z_{top}} [\theta_{sl} - \theta(z)]\, dz\right]^{-1}, \tag{5.36}$$

where k_e again is the entrainment coefficient. The value of k_e can be viewed schematically as the ratio of negative area to positive area within the planetary boundary layer in Fig. 5.13.

Results from Zhang and Anthes (1982) suggest that this non-local scheme typically does very well in non-saturated boundary layers. Bright and Mullen (2002) also find that it does very well in simulating the boundary layers over

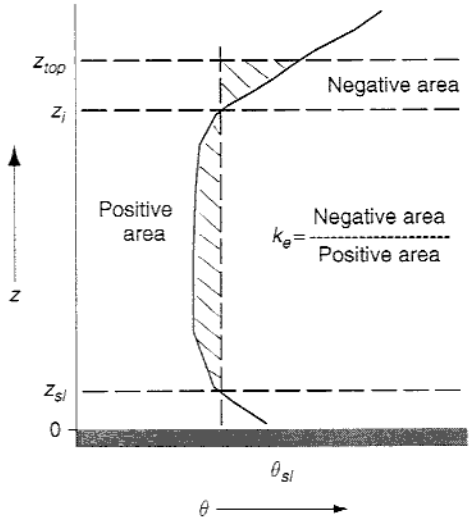

Figure 5.13. Illustration of potential temperature versus height within the boundary layer, highlighting the positive and negative areas on the diagram that are used to define the boundary layer top (z_{top}). The entrainment coefficient is k_e and z_i is the inversion level. After Zhang and Anthes (1982).

Arizona during the summertime, when boundary layer depths can exceed 3 km. As applied in numerical models, this scheme reverts to a local closure approach during neutral and stable boundary layer conditions. An extension of this scheme that retains the direct, non-local upward flux from rapidly rising plumes while also including a gradual downward flux due to compensatory subsidence is found in Pleim and Chang (1992).

5.4.3 Non-local diffusion scheme

Another non-local closure approach to modeling the boundary layer is used in the National Centers for Environmental Prediction (NCEP) Global Forecast System (GFS). This scheme is described by Hong and Pan (1996), based upon Troen and Mahrt (1986), and the description of it here largely follows their derivation. This scheme uses results from large-eddy simulations in its formulation. Deardorff (1972), Troen and Mahrt (1986), Holtslag and Moeng (1991) and Holtslag and Boville (1993) show that the turbulence diffusion equations for prognostic variables (u, v, θ, q) can be expressed as

$$\frac{\partial C}{\partial t} = \frac{\partial}{\partial z}\left[K_c\left(\frac{\partial C}{\partial z} - \gamma_c\right)\right], \tag{5.37}$$

where K_c is the eddy diffusivity coefficient and γ_c is a correction to the local gradient that incorporates the contributions of the large-scale eddies. In this scheme, the correction to the local gradient only applies to the potential temperature and specific humidity equations, and not to momentum. In addition, a local closure approach is used above the boundary layer.

Following Troen and Mahrt (1986), Holtslag *et al.* (1990), and Holtslag and Boville (1993), the momentum diffusivity coefficient is defined as

$$K_{zm} = kzw_s\left(1 - \frac{z}{h}\right)^2, \tag{5.38}$$

where k is the von Karman constant ($=0.4$), z is the height above the ground surface, h is the height of the boundary layer, w_s is the mixed layer velocity scale, and the exponent 2 is a profile shape parameter. The mixed layer velocity scale is defined as

$$w_s = u_* \phi_m^{-1}, \tag{5.39}$$

where u_* is the surface friction velocity and ϕ_m is the wind profile function evaluated at the top of the surface layer. The correction to the local gradient from the large-scale eddies for θ and q is given by

$$\gamma_c = 7.8 \frac{\overline{(w'c')_{sfc}}}{w_s}. \tag{5.40}$$

Here the constant 7.8 is a proportionality constant defined following the derivation in Troen and Mahrt (1986). To ensure that the top of the surface layer and the bottom of the boundary layer are compatible, identical profile functions are used for both layers. For unstable and neutral conditions, defined as having positive buoyancy flux, define

$$\phi_m = \left(1 - 16\frac{0.1h}{L}\right)^{-1/4}, \tag{5.41}$$

$$\phi_t = \left(1 - 16\frac{0.1h}{L}\right)^{-1/2}, \tag{5.42}$$

where L is the Monin–Obukhov length, ϕ_m is used for momentum variables, and ϕ_t is used for mass variables. For the stable regime with buoyancy fluxes less than zero, the profile functions are defined as

$$\phi_m = \phi_t = \left(1 + 5\frac{0.1h}{L}\right). \tag{5.43}$$

Finally, to close the system the boundary layer height is calculated from

$$h = Ri_c \frac{\theta_{v_a} |U(h)|^2}{g(\theta(h) - \theta_s)}, \tag{5.44}$$

where Ri_c is the critical Richardson number ($=0.25$), $U(h)$ is the horizontal wind speed at the top of the boundary layer (h), θ_{v_a} is the virtual potential temperature at the first model level above the ground surface, and θ_s is a near-surface temperature defined as

$$\theta_s = \theta_{v_a} + \theta_T = \theta_{v_a} + 7.8 \frac{\overline{(w'\theta'_v)_{sfc}}}{w_s h}. \tag{5.45}$$

In the early testing of this scheme, it was found that the value of θ_T could become too large when the winds were weak, yielding an unrealistically large boundary layer depth, so an upper value of $\theta_T = 3.0$ was chosen. In addition, the thermal diffusivity coefficient K_{zt} is proportional to the value of K_{zm} through the Prandtl number (Pr), such that

$$Pr = \frac{K_{zm}}{K_{zt}} = \left(\frac{\phi_t}{\phi_m} + 7.8k \frac{0.1h}{h} \right). \tag{5.46}$$

The value for boundary layer height (h) is determined iteratively. First, h is estimated without considering the thermal excess θ_T. This value of h is then used to compute all other variables needed, and then to compute the thermal excess. Then h is calculated again using the value for θ_T. This is done until a value for h is found that is stable.

The scheme perhaps is easier to understand if one rewrites the equation for boundary layer height in terms of the virtual potential temperature at the boundary layer top. This manipulation yields

$$\theta_v(h) = \theta_{v_a} + \theta_T + \frac{Ri_c \theta_{v_a} |U(h)|^2}{gh}. \tag{5.47}$$

From here it is easier to see that as the buoyancy flux from the ground surface increases, leading to a larger value of θ_T, the boundary layer deepens since $\theta_v(h)$ increases (see Fig. 5.14). The third term shows that $\theta_v(h)$ increases as the wind speed at the top of the boundary layer increases and is larger for smaller boundary layer depths. These behaviors are consistent with many observations of boundary layer development.

Results from Hong and Pan (1996) indicate that this non-local diffusion scheme produces better boundary layer structures during the First ISLSCP (International Satellite Land Surface Climatology Project) Field Experiment

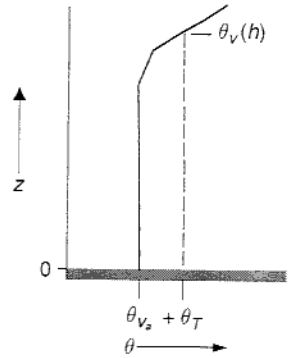

Figure 5.14. Boundary layer potential temperature versus height, showing the relationship between surface layer $\theta_{v_s} + \theta_T$ and the temperature at the top of the boundary layer $\theta_v(h)$.

(FIFE) than a local closure scheme (Fig. 5.15). The local closure scheme for this case produces a boundary layer that is too shallow, which is a well-known problem when countergradient fluxes are important. The non-local diffusion scheme produces an adiabatic lapse rate in the boundary layer, very much in agreement with observations. In addition, while the non-local scheme underestimates the specific humidity near local noon, it produces a very reasonable moisture profile by late afternoon (Fig. 5.15).

There are many other non-local closure schemes available in the literature. One of the more unique schemes is from Stull (1984, 1988, 1993) who develops a transilient turbulence scheme that allows for a range of eddy sizes to influence the turbulent mixing. This theory is based upon a discrete view of the non-local mixing that occurs in the boundary layer. Consider a boundary layer that is divided into a finite set of discrete layers, which for simplicity are assumed to have equal depth. Since large eddies dominate the vertical mixing in many boundary layers, it is possible that the evolution of a given vertical layer is influenced by mixing with any or all of the other vertical layers. Thus, there is a need to represent how each layer mixes with each other layer. This is accomplished by defining a transilient matrix $c(i, j)$ to represent the fraction of air mixed into vertical layer i from vertical layer j.

The transilient matrix has a number of constraints in order to satisfy mass and state conservation. The sum of all the values of $c(i, j)$ for a fixed value of j must equal 1, and the sum of all the mass-weighted values of $c(i, j)$ for a fixed value of i must equal 1. In addition, no element can have a value less than 0 or greater than 1. As an example, if no vertical mixing occurs, then the diagonal elements of $c(i, j)$ are equal to 1 and all the other elements are equal to zero,

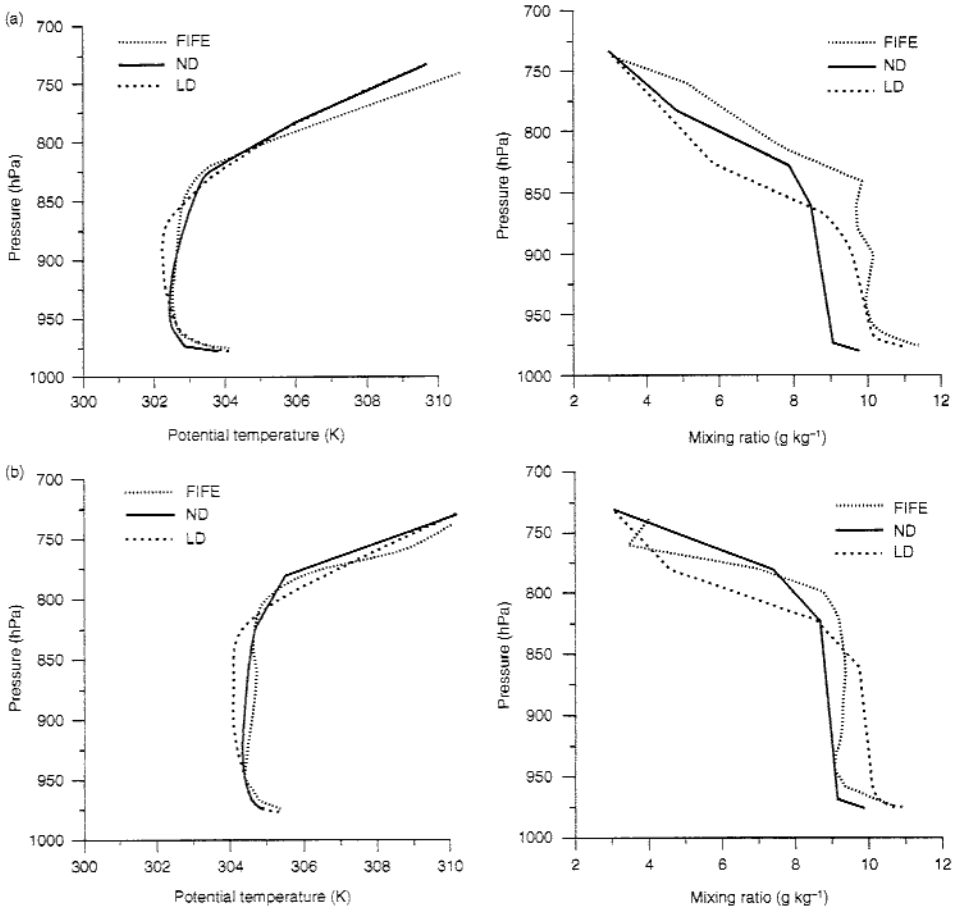

Figure 5.15. Comparisons of boundary layer profiles of potential temperature (K) and mixing ratio ($g\,kg^{-1}$) for the 9–10 August sonde averages (shaded lines) with averages from the non-local (solid lines) and local (dotted lines) schemes for (a) 1845 UTC and (b) 2145 UTC. Potential temperature on the left side, and mixing ratio on the right-hand side of the figure. From Hong and Pan (1996).

indicating that no mixing occurs. In contrast, if all the elements of $c(i, j)$ are non-zero, then the boundary layer is mixing throughout its depth.

A variety of different physical processes can be simulated with this approach depending on the form of the transilient matrix. The mixing processes active at any given time can be discerned from the location within the transilient matrix and the amount of air involved as indicated by the size of the matrix elements (Fig. 5.16). This scheme unifies the boundary layer and turbulence parameterizations under a single approach. Raymond and Stull (1990) apply this unified turbulence scheme to several case studies and show good results.

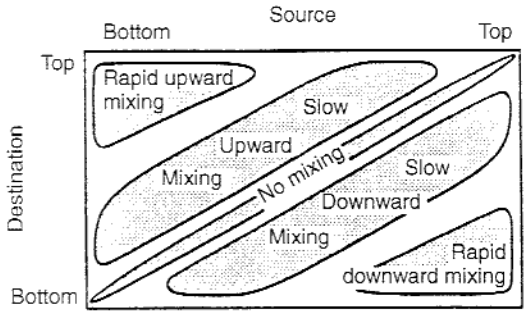

Figure 5.16. Physical interpretation of the mixing processes from the elements in a transilient matrix. The amount of air involved in the mixing is determined by the magnitudes of the elements. From Ebert *et al.* (1989).

5.5 Local closure schemes

The discussion of non-local closure schemes suggests that there are problems with local closure schemes, since the local stability is not necessarily related to the amount of turbulence and mixing that is occurring. This mixing is often tied strongly to the largest eddies present within the boundary layer, which are not controlled by local gradients in stability. Methods to overcome these deficiencies in local closure involve using higher-order local closures (Mellor and Yamada 1982). However, we begin by reviewing the concepts of first-order closure before moving on to more sophisticated schemes.

5.5.1 First-order closure scheme

One of the most commonly used forms of turbulent closure is first-order closure, commonly referred to as K-theory. In first-order closure, only the prognostic equations for the means of the variables are retained and the turbulent fluxes are parameterized (Stull 1988). Thus, we begin with

$$\frac{\partial \bar{u}_i}{\partial t} + \bar{u}_j \frac{\partial \bar{u}_i}{\partial x_j} = -\delta_{i3} g + f \varepsilon_{ijk} \bar{u}_j - \frac{1}{\bar{\rho}} \frac{\partial \bar{p}}{\partial x_i} + \nu \frac{\partial^2 \bar{u}_i}{\partial x_j{}^2} - \frac{\partial \overline{(u_i' u_j')}}{\partial x_j}, \tag{5.48}$$

$$\frac{\partial \bar{\theta}}{\partial t} + \bar{u}_j \frac{\partial \bar{\theta}}{\partial x_j} = -\frac{\partial \overline{(u_j' \theta')}}{\partial x_j} + \text{diabatic terms}, \tag{5.49}$$

$$\frac{\partial \bar{q}}{\partial t} + \bar{u}_j \frac{\partial \bar{q}}{\partial x_j} = -\frac{\partial \overline{(u_j' q')}}{\partial x_j} + \text{source/sink terms}, \tag{5.50}$$

where the covariance terms are those that need to be parameterized. Note that on the right-hand side of (5.48), the second to last term represents molecular effects and is so small that it can be neglected. The covariance terms are parameterized using

$$\overline{u_j'\zeta'} = -K\frac{\partial\bar{\zeta}}{\partial x_j}. \tag{5.51}$$

where K has units of $m^2 s^{-1}$. For $K>0$, the flux $\overline{u_j'\zeta'}$ flows down the local gradient of $\bar{\zeta}$. This relationship is called K-theory. If we use this relationship in the equations for the mean quantities, then we obtain

$$\frac{\partial\bar{u}_i}{\partial t} + \bar{u}_j\frac{\partial\bar{u}_i}{\partial x_j} = -\delta_{i3}g + f\varepsilon_{ijk}\bar{u}_j - \frac{1}{\bar{\rho}}\frac{\partial\bar{p}}{\partial x_i} + K_m\frac{\partial^2\bar{u}_i}{\partial x_j^2}, \tag{5.52}$$

$$\frac{\partial\bar{\theta}}{\partial t} + \bar{u}_j\frac{\partial\bar{\theta}}{\partial x_j} = K_H\frac{\partial^2\bar{\theta}}{\partial x_j^2} + \text{diabatic terms}, \tag{5.53}$$

$$\frac{\partial\bar{q}}{\partial t} + \bar{u}_j\frac{\partial\bar{q}}{\partial x_j} = K_H\frac{\partial^2\bar{q}}{\partial x_j^2} + \text{source/sink terms}. \tag{5.54}$$

where K_m and K_H are the different coefficients for the mixing of momentum and mass, respectively. Typically, when one refers to K-theory they only mean the vertical derivatives and the horizontal derivatives are referred to as horizontal diffusion.

It is often helpful to view this relationship schematically. To begin, look at the $\overline{w'\theta'}$ term since we have some idea how this flux behaves in the planetary boundary layer. As shown in Fig. 5.17, if θ decreases with height as occurs in the lowest portion of the boundary layer, then $\overline{w'\theta'}$ is positive and turbulence

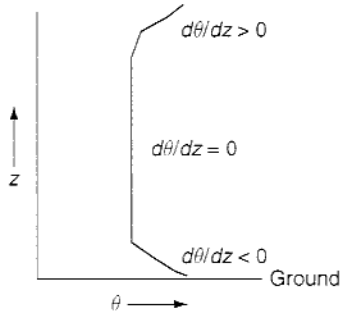

Figure 5.17. Illustration of the boundary layer potential temperature versus height, with the lapse rates for three very different layers indicated.

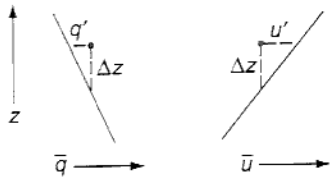

Figure 5.18. Profiles of and $\bar{q}$ and $\bar{u}$ (solid lines) as a function of z. The perturbations q' and u' are created by moving a parcel upward within this environment an amount Δz.

moves warm air upward. This is consistent with expectations from rising thermals moving hot air near the ground upward. If θ increases with height, as occurs at the very top of the boundary layer, then $\overline{w'\theta'}$ is negative and turbulence moves warm air downward. This is what one would expect from the entrainment of warmer air from aloft into the boundary layer. However, a problem occurs when θ is constant with height as occurs in the middle of a very well-mixed layer during the daytime. In this case, K-theory indicates that no turbulence is occurring, whereas observations would probably show very strong thermals moving upward through the boundary layer and penetrating the capping inversion.

A simple thought experiment can be used to illustrate a variation on K-theory. Assume that an idealized boundary layer exists with linear profiles of q and u as in Fig. 5.18, where only small eddies are present (i.e., no non-local transport). A turbulent eddy moves a parcel upward a distance of Δz and the parcel does not mix with the surrounding environment. Thus, the parcel differs from its environment by

$$q' = -\left(\frac{\partial \bar{q}}{\partial z}\right)\Delta z, \tag{5.55}$$

$$u' = -\left(\frac{\partial \bar{u}}{\partial z}\right)\Delta z. \tag{5.56}$$

Now, in order to move a distance Δz, the parcel requires some upward motion w'. If the turbulence is such that w' is proportional to u', then

$$w' = -cu' = c\left(\frac{\partial \bar{u}}{\partial z}\right)\Delta z. \tag{5.57}$$

From the equations above, the product $w'q'$ caused by that one idealized eddy can be determined. Averaging over many such eddies to find $\overline{w'q'}$ yields

$$\overline{w'q'} = -\overline{\left(\frac{\partial \bar{q}}{\partial z}\right)\Delta z c\left(\frac{\partial \bar{u}}{\partial z}\right)\Delta z} = -c\overline{(\Delta z)^2}\left(\frac{\partial \bar{q}}{\partial z}\right)\left(\frac{\partial \bar{u}}{\partial z}\right), \tag{5.58}$$

where $\overline{(\Delta z)^2}$ is the variance of the parcel displacement. If a mixing-length l is defined, such that $l^2 = c\overline{(\Delta z)^2}$ then

$$\overline{w'q'} = -l^2\left|\frac{\partial \bar{u}}{\partial z}\right|\frac{\partial \bar{q}}{\partial z}. \tag{5.59}$$

Recalling from K-theory that

$$\overline{w'q'} = -K_H\frac{\partial \bar{q}}{\partial z}, \tag{5.60}$$

then it follows that

$$K_H = l^2\left|\frac{\partial \bar{u}}{\partial z}\right|, \tag{5.61}$$

which is called mixing-length theory (Stull 1988). This theory suggests that K increases as the shear increases, and also that K increases as the variance of the parcel displacement increases. This allows for K-theory to apply in a more realistic way to boundary layer development. The limitations of mixing-length theory are that it is valid only in boundary layers not having large eddies, and that it only allows for downgradient transport (unless $K < 0$ is allowed). Also note that the vertical transport of perturbation velocities is neglected, which may be large.

Let us return again to examine observations and compare against mixing-length theory. It is not unusual for the winds within the boundary layer to be relatively constant with height within a well-mixed layer during the daytime (Fig. 5.19). This situation often occurs when large eddies are present, which implies mixing-length theory will have difficulty. Zhang and Anthes (1982) show the development of such a mixed layer over Marfa, Texas, at both 1800 UTC 10 April and 0000 UTC 11 April 1979. Using mixing-length theory, an examination of Fig. 5.19 suggests that the value of K_H is again near zero throughout the boundary layer, and then changes to a large value at the top of the boundary layer where the wind shear is greatest. So, K_H from mixing-length theory is influenced by dU/dz, but not by the stability of the layer. This is not realistic, and indicates that more reasonable parameterizations for K are needed. Blackadar (1979) suggests that one such parameterization valid for heights less than 200 m is

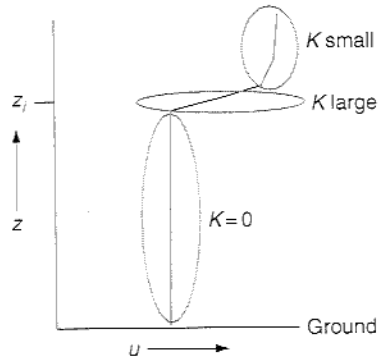

Figure 5.19. Mean wind speed u versus height z within a daytime boundary layer from the ground surface to above the inversion level (z_i). Values of K indicated within three different layers.

$$K_H = 1.1\left[\frac{(Ri_c - Ri)l^2}{Ri}\right]\left|\frac{\partial \bar{u}}{\partial z}\right|, \tag{5.62}$$

where Ri is the Richardson number defined as

$$Ri = \frac{(g/\theta_v)(\partial \bar{\theta}_v/\partial z)}{(\partial \bar{u}/\partial z)^2}, \tag{5.63}$$

and $l = kz = 0.4z$. For heights greater than 200 m, one might instead use

$$K_H = (1 - 18Ri)^{-1/2} l^2 \left|\frac{\partial \bar{u}}{\partial z}\right|, \tag{5.64}$$

where $l = 70$ m and K_H cannot be negative (Stull 1988).

One of the common threads in these various definitions of K is that they depend only upon the local values of the model variables, such that K-theory is a local closure approach to turbulence closure. Because of the local closure assumption, when surface heating is strong, K-theory can produce very deep superadiabatic layers near the surface that are unrealistic. In addition, not all turbulent transport is downgradient. This last point can easily be illustrated by examining the boundary layer during a typical summer morning. A superadiabatic layer exists near the ground surface, with the remaining stable nocturnal inversion layer above it. Large eddies associated with the rise of warm air parcels transport heat from hot to cold regardless of the local gradient of the background environment. So in this case warm thermals move heat upward, even though the background environment would suggest from K-theory that warm air is being transported downward. Thus, when large eddies exist, K-theory often fails owing to upgradient, or countergradient,

fluxes. This is perhaps the most important criticism of K-theory – that the mass and momentum transport in the boundary layer during the daytime is mostly accomplished by the largest eddies, and that these eddies are more representative of the properties of the entire boundary layer than the local conditions at one vertical level (Deardorff 1972; Troen and Mahrt 1986; Holtslag and Moeng 1991; Stull 1991). In addition, Ayotte *et al.* (1996) show that this type of scheme tends to underestimate entrainment when the capping inversion is strong.

5.5.2 1.5-order local closure scheme

As the order of the closure increases, the parameterizations include more equations for the higher moments. Thus, for 1.5-order closure the parameterizations typically include equations not only for the standard prognostic variables ($\overline{u}$, $\overline{v}$, $\overline{\theta}$, $\overline{q}$), but also the potential temperature variance ($\overline{\theta'^2}$) and the turbulent kinetic energy ($\overline{e}$). Also recall that most boundary layer schemes in use today are one-dimensional and only consider the vertical derivatives. The equations for a typical 1.5-order closure scheme are (Stull 1988)

$$\frac{\partial \overline{u}_i}{\partial t} + \overline{u}_j \frac{\partial \overline{u}_i}{\partial x_j} = -\delta_{i3} g + f \varepsilon_{ijk} \overline{u}_j - \frac{1}{\overline{\rho}} \frac{\partial \overline{p}}{\partial x_i} - \frac{\partial \overline{(u_i' w')}}{\partial z}. \tag{5.65}$$

$$\frac{\partial \overline{\theta}}{\partial t} + \overline{u}_j \frac{\partial \overline{\theta}}{\partial x_j} = -\frac{\partial \overline{(w'\theta')}}{\partial z} + \text{diabatic terms.} \tag{5.66}$$

$$\frac{\partial \overline{q}}{\partial t} + \overline{u}_j \frac{\partial \overline{q}}{\partial x_j} = -\frac{\partial \overline{(w'q')}}{\partial z} + \text{source/sink terms.} \tag{5.67}$$

$$\frac{\partial \overline{e}}{\partial t} = -\overline{u'w'} \frac{\partial \overline{u}}{\partial z} - \overline{v'w'} \frac{\partial \overline{v}}{\partial z} + \frac{g}{\overline{\theta}} \overline{w'\theta'} - \frac{\partial}{\partial z} \overline{\left(\frac{w'p'}{\rho} + ew' \right)} - \varepsilon, \tag{5.68}$$

$$\frac{\partial \overline{\theta'^2}}{\partial t} = -2\overline{w'\theta'} \frac{\partial \overline{\theta}}{\partial z} - \frac{\partial}{\partial z} \left(\overline{w'\theta'^2} \right) - 2\varepsilon_\theta - \varepsilon_R, \tag{5.69}$$

where dissipation is indicated by the ε, ε_θ, and ε_R terms.

The unknown variables in this set of equations include the fluxes $\overline{u'w'}$, $\overline{v'w'}$, $\overline{w'\theta'}$, $\overline{w'p'}/\overline{\rho}$, and $\overline{w'q'}$, the third moments $\overline{w'e}$, $\overline{w'\theta'^2}$, and the three dissipation terms. Thus, as mentioned by Stull (1988), it initially appears that the addition of the variance equations has created havoc instead of

producing conceptual stability. With first-order closure there are four unknowns to specify, whereas here there are six more unknowns for a total of 10! The reason behind this apparent madness is that the additional equations for the potential temperature variance and the turbulent kinetic energy provide information on the intensity and effectiveness of the turbulence within the boundary layer. This information is used to develop improved parameterizations for the eddy diffusivities K that can now be functions of $\overline{\theta'^2}$ and $\bar{e}$ instead of just functions of wind shear and stability as developed for first-order closure.

Following Yamada and Mellor (1975), one suggested set of parameterizations for the 10 unknowns is as follows:

$$\overline{u'w'} = -K_m\left(\bar{e}, \overline{\theta'^2}\right)\frac{\partial \bar{u}}{\partial z}, \tag{5.70}$$

$$\overline{v'w'} = -K_m\left(\bar{e}, \overline{\theta'^2}\right)\frac{\partial \bar{v}}{\partial z}, \tag{5.71}$$

$$\overline{w'\theta'} = -K_H\left(\bar{e}, \overline{\theta'^2}\right)\frac{\partial \bar{\theta}}{\partial z} - \gamma_c\left(\bar{e}, \overline{\theta'^2}\right), \tag{5.72}$$

$$\overline{w'q'} = -K_H\left(\bar{e}, \overline{\theta'^2}\right)\frac{\partial \bar{q}}{\partial z} - \gamma_c\left(\bar{e}, \overline{\theta'^2}\right), \tag{5.73}$$

$$\overline{w'\left(\frac{p'}{\bar{\rho}} + e\right)} = \frac{5}{3}L_4 e^{-1/2}\frac{\partial \bar{e}}{\partial z}, \tag{5.74}$$

$$\overline{w'\theta'^2} = -L_3 e^{1/2}\frac{\partial \overline{\theta'^2}}{\partial z}, \tag{5.75}$$

$$\varepsilon = \frac{\bar{e}^{3/2}}{L_1}, \tag{5.76}$$

$$\varepsilon_R = 0, \tag{5.77}$$

$$\varepsilon_\theta = \frac{\bar{e}^{1/2}\overline{\theta'^2}}{L_2}. \tag{5.78}$$

Here L_x are empirical length-scale parameters that are often chosen by trial and error to make the simulated flow best match the observed flow for a given

set of cases. Often the values of L approach kz for small z, and approach a specified constant L_0 for large z. Typically, values for L_0 are between 50 and 100 m. Also, the γ_c term is used so that flux occurs even when there is no mean vertical gradient in the variable, thereby allowing countergradient fluxes.

The expressions for the eddy diffusivities K are complex and include terms related to the environmental wind shear and stability, but can be represented in conceptual form as

$$K = L\sqrt{\bar{e}}, \tag{5.79}$$

where L is again one of the empirical length scales. Further information on the details of these types of closure schemes can be found in Mellor and Yamada (1982) and Janjic (1994). Another approach to determining the empirical length scale is to include a separate prognostic equation for the dissipation rate ε that is then used with the turbulent kinetic energy to calculate the length scales (Stull 1988). However, these e–ε closure schemes are not very prevalent in the meteorological literature.

Note that in the parameterizations of the unknowns a consistency is seen that applies for almost all of the definitions – downgradient diffusion. The parameterizations for the covariance terms are specified as functions of the vertical gradients of the mean variables, i.e. the $\overline{w'\theta'}$ term is related to the vertical gradient of $\bar{\theta}$, and the value of K_H depends upon the potential temperature variance and the turbulent kinetic energy. Similarly, the triple correlation terms are parameterized as flowing down the vertical gradients of the covariances, i.e. the $\overline{w'\theta'^2}$ term is related to the vertical gradient of $\overline{\theta'^2}$ and the magnitude of the turbulent kinetic energy. Note also that the dissipation terms are parameterized as being proportional to their respective variables. Thus, as the turbulent kinetic energy increases, its dissipation also increases.

The ability of 1.5-order and higher closure schemes to account for countergradient fluxes is shown by Deardorff (1966). In the thermal variance equation (5.69), the first term on the right-hand side is a production term that increases the thermal variance when the heat flux is downgradient, while the dissipation terms act to smooth the flow. It is the second term on the right-hand side that allows for countergradient flux. Deardorff (1966) notes that $\overline{w'\theta'}$ is generally large when $\theta' > 0$ in the boundary layer and small otherwise, so $\overline{w'\theta'^2}$ is positive but decreases with height in the countergradient region. This situation leads to countergradient fluxes as the thermal variance is increased.

One would expect that countergradient fluxes would be particularly important in dry convective boundary layers. Teixeira *et al.* (2004) develop and test a 1.5-order closure scheme that shows improvements in simulating dry

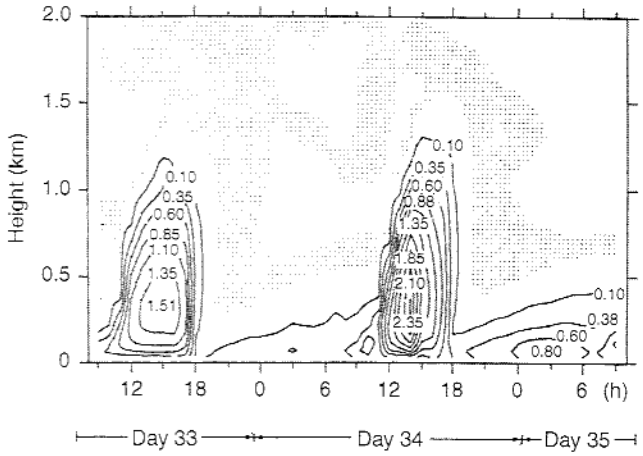

Figure 5.20. Time and vertical variation of the computed $\bar{e}^2$ (twice the turbulent kinetic energy in $m^2 s^{-2}$) for days 33–35 of the Wangara experiment. From Yamada and Mellor (1975).

convective boundary layers over southern Portugal. Results suggest that the improved boundary layer predictions are due to more realistic representations of entrainment.

One of the benefits of 1.5-order or higher closure schemes is that they explicitly predict the intensity of the turbulent kinetic energy (Fig. 5.20). The diurnal cycle of the boundary layer is clearly seen in the turbulent kinetic energy, and this type of information may be useful in studies of air pollution dispersion. As discussed by Yamada and Mellor (1975), the computed turbulence field helps to explain the behavior of the mean quantities, even if it is difficult to use in comparisons with observations of turbulence.

The NCEP Eta model uses a 1.5-order closure scheme (Janjic 1994) for the boundary layer that is slightly different from that discussed above. In the Eta model scheme there is no equation for the potential temperature variance, so the eddy diffusivities are defined only in terms of the turbulent kinetic energy. This highlights that one must be careful when discussing schemes with non-integer closures, since the exact application of the intermediate closure assumptions is uncertain.

5.5.3 Second-order closure scheme

The many details involved in a full second-order closure scheme can be found in Mellor and Yamada (1982) and Stull (1988), which are both excellent sources for information on local closure schemes. In addition to the equations

listed for 1.5-order closure, second-order closure also has predictive equations for all the remaining covariance terms $\overline{u_i'u_j'}$, $\overline{u_j'\theta'}$, and $\overline{u_j'q'}$. The number of unknowns is large and includes some very complex and rather daunting-looking terms. For example, if we look at the time rate of change of the momentum covariance term we find

$$\frac{\partial\overline{(u_i'u_j')}}{\partial t} = -\overline{u_j'w'}\frac{\partial\bar{u}_j}{\partial z} - \overline{u_j'w'}\frac{\partial\bar{u}_i}{\partial z} - \frac{\partial\overline{(u_i'u_j'w')}}{\partial z} + \frac{g}{\bar{\theta}}\left(\delta_{i3}\overline{u_j'\theta'} + \delta_{j3}\overline{u_i'\theta'}\right) + \overline{\left(\frac{p'}{\rho}\right)\left(\frac{\partial u_i'}{\partial x_j} + \frac{\partial u_j'}{\partial x_i}\right)} - 2\varepsilon_{u_iu_j}. \tag{5.80}$$

This equation has a triple correlation term and a pressure correlation term. The pressure correlation term

$$\overline{\left(\frac{p'}{\rho}\right)\left(\frac{\partial u_i'}{\partial x_j} + \frac{\partial u_j'}{\partial x_i}\right)}. \tag{5.81}$$

partitions energy among the three components while not contributing to the total energy. Rotta (1951) provides a key suggestion for the parameterization of this term by calling it an "energy redistribution term" and specifying it as being

$$\overline{\left(\frac{p'}{\rho}\right)\left(\frac{\partial u_i'}{\partial x_j} + \frac{\partial u_j'}{\partial x_i}\right)} = c\overline{u_i'u_j'} + d\frac{\partial\bar{u}_i}{\partial x_j}, \tag{5.82}$$

where c and d are constants. There are many proposed ways to parameterize the various terms in higher-order closure schemes. Most use some variant of mixing-length theory and Monin–Obukhov similarity theory as a foundation. Examples can be found in Launder *et al.* (1975), Lumley and Khajeh-Nouri (1974), Mellor and Yamada (1974), Rotta (1951), Zeman (1981), and Wichmann and Schaller (1986). Others are undoubtedly given in the literature. While it is nearly impossible to summarize all the proposed parameterizations, a brief overview of some commonly used closures is helpful.

The downgradient diffusion model suggests that

$$\frac{\partial\overline{(w'e)}}{\partial z} = -\frac{\partial}{\partial z}\left(L_1\sqrt{\bar{e}}\frac{\partial\bar{e}}{\partial z}\right), \tag{5.83}$$

where L_1 is another empirical length scale. As mentioned previously, downgradient diffusion models have difficulty in simulating convective boundary layers where large eddies are important.

The diffusion term ε can be parameterized as

$$\varepsilon = \frac{\bar{e}^{3/2}}{L_2}, \tag{5.84}$$

which is obtained through scaling arguments (Mellor and Yamada 1982). L_2 is another empirical length scale.

The triple correlation terms can also be parameterized using the down-gradient diffusion model, such that

$$\frac{\partial \overline{w'^2\theta'}}{\partial z} = -\frac{\partial}{\partial z}\left[L_3\sqrt{\bar{e}}\frac{\partial(\overline{w'\theta'})}{\partial z}\right], \tag{5.85}$$

$$\frac{\partial \overline{w'\theta'^2}}{\partial z} = -\frac{\partial}{\partial z}\left[L_4\sqrt{\bar{e}}\frac{\partial(\overline{\theta'^2})}{\partial z}\right], \tag{5.86}$$

where L_3 and L_4 are two more empirical length scales. Typically, one finds that

$$(L_1, L_2, L_3, L_4, \ldots) = (\alpha_1, \alpha_2, \alpha_3, \alpha_4, \ldots)L, \tag{5.87}$$

where

$$L = \frac{kz}{1 + kz/L_0}, \tag{5.88}$$

and

$$L_0 = \frac{0.1\int_0^{z_i}\sqrt{\bar{e}}z\,dz}{\int_0^{z_i}\sqrt{\bar{e}}\,dz}. \tag{5.89}$$

In their review of local closure schemes, Mellor and Yamada (1982) state that "the major weakness of all the models probably relates to the turbulent master length scale (or turbulent macroscale, or turbulent inertial scale), and, most important, to the fact that one sets all process scales proportional to a single scale." A comparison of a second-order closure simulation to observations during 2 days of the Wangara experiment shows that the boundary layer scheme reproduces the general evolution of the boundary layer very well, yet some important differences between the simulation and observations are also seen (Fig. 5.21). At 12 local time the simulated boundary layer shows the mean virtual potential temperature decreasing with height up to just below 1 km, whereas observations indicate a nearly constant value up to above 1 km. The boundary layer depth at 18 local time remains near 1 km in the simulation, but is closer to 1.25 km in the observations. The simulated and observed profiles at 3 and 9 local time agree fairly well, indicating that the local closure approach does well at reproducing the nocturnal boundary layer structures for this case.

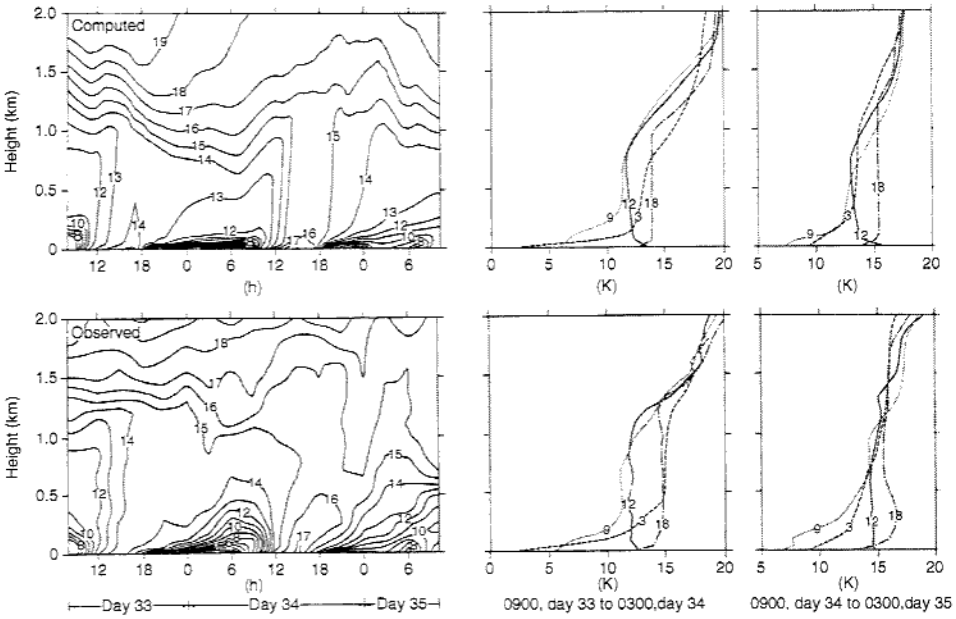

Figure 5.21. Simulated (top) and observed (bottom) boundary layer virtual potential temperature (θ_v) and vertical and temporal variations taken during the Wangara experiment over Hays, Australia. Isolines on the left-hand plot are $\theta_v - 273$ and shown in units of kelvin. Times indicated on the right-hand plots are local. From Yamada and Mellor (1975).

Thus, as mentioned previously, the local closure approach may have difficulties in predicting the daytime convective boundary layer, although it does a reasonable job in reproducing the nocturnal boundary layer for this case.

5.6 Turbulence and horizontal diffusion

Above the planetary boundary layer, turbulence and vertical mixing still occur and need to be represented in numerical models. Local closure schemes typically are used to calculate mixing throughout the vertical extent of the model domain from the surface through the PBL and upwards to the model top. Transilient turbulence theory also handles turbulence both in and above the boundary layer, in addition to predicting boundary layer depth. Other non-local closure schemes often are developed only to determine the PBL depth, and another closure approach is used above the PBL to account for turbulent mixing. For example, Zhang and Anthes (1982) use a non-local closure scheme to represent daytime penetrative convection, but a first-order local closure scheme is used above the PBL and under stable conditions at night. Thus, some models mix both non-local and local closure schemes depending upon whether

the PBL is unstable, neutral, or stable, in order to provide the best predictions of boundary layer structure. Also, some numerical models have numerical stability problems, and sometimes the numerical noise is damped by increasing K to values that are much larger than is physically reasonable.

Horizontal diffusion is used in numerical models to parameterize not only the horizontal effects of turbulent mixing but also to help control aliasing and non-linear instabilities. Many models use either a second-order or a more scale-selective fourth-order form for the diffusion term. The diffusion coefficient often has a constant background value plus a second term proportional to the horizontal deformation (Smagorinsky *et al.* 1965; Anthes and Warner 1978). Horizontal diffusion typically is calculated on the model coordinate surfaces, although studies indicate that this approach may cause problems in regions of complex terrain if the model coordinates are terrain following (Zängl 2002; Juang *et al.* 2005). The form of the horizontal diffusion term may be time-step-dependent, producing sensitivities to the value of the model time step in the predicted precipitation fields for a weakly forced large-scale environment (Xu *et al.* 2001).

5.7 Discussion

The evolution of the planetary boundary layer is very important, as it sets the stage for many of the sensible weather phenomena that can occur in the atmosphere, such as deep convection. Yet predicting the development and evolution of the boundary layer is quite challenging, since the dominant mechanism for boundary layer development is turbulence. During the daytime, turbulence is often dominated by buoyancy gradients produced by surface forcing. However, at night and in certain environments, turbulence is created from the shear of the mean wind profile and is intermittent. Boundary layer schemes, of course, have to account for all of these mechanisms by which turbulence is generated, which is not a trivial task.

In contrast, it is easy to see that the magnitudes of the surface sensible and latent heat fluxes are important to the boundary layer scheme during the daytime when solar insolation dominates the surface energy budget. At night, the balance between the incoming and outgoing longwave radiation plays a large role in determining the evolution of the boundary layer, as does the mean wind profile. The connections between the boundary layer and the soil–vegetation–atmosphere schemes discussed in Chapter 3 are many and multifaceted. It is not difficult to imagine the complexities and sensitivities one may encounter in boundary layer evolutions around the world that could lead any scheme to reproduce the observed boundary layer poorly on a given

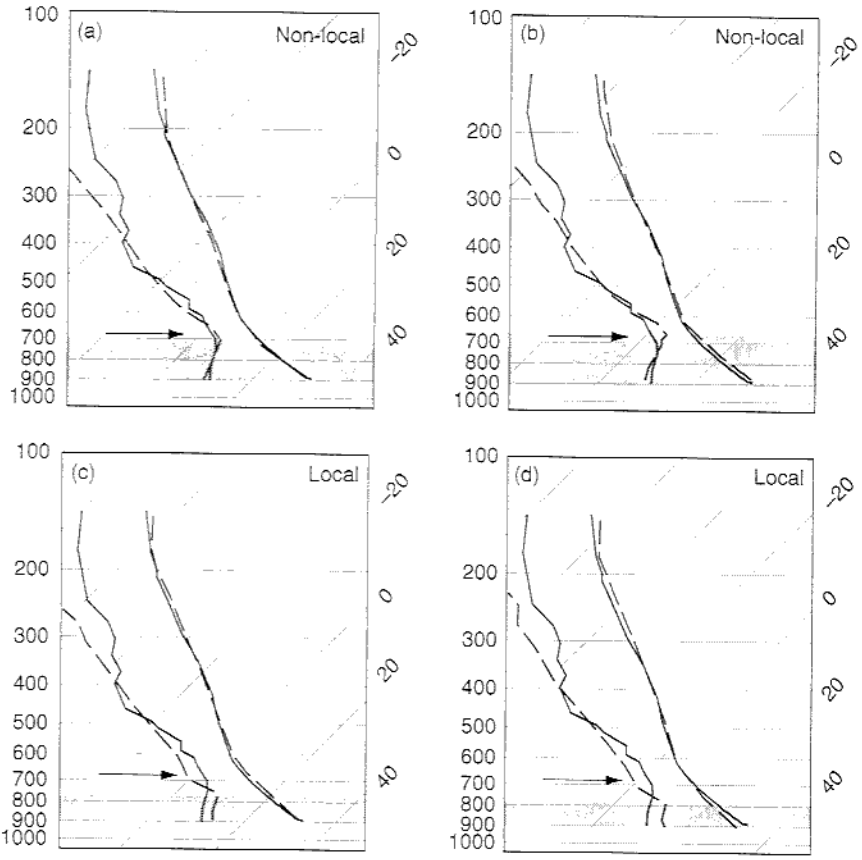

Figure 5.22. Skew-T log p plot of 0000 UTC observed (solid) and 12 h forecast (dashed) composite soundings for Tucson, Arizona, for (a, b) non-local closure schemes and (c, d) local closure schemes. Gray shading indicates model-predicted PBL depths, while the arrow indicates the estimated PBL depth from the observed composite sounding. Notice how both local closure schemes underpredict the depth of the boundary layer by roughly half. After Bright and Mullen (2002).

day. However, it also appears that certain boundary layer scheme behaviors are consistent over time. For example, Bright and Mullen (2002) show that the local closure schemes consistently underpredict the boundary layer depth over Arizona during the summertime (Fig. 5.22). This results in boundary layers that are too cool and moist. During this time of year, boundary layer depths are typically greater than 2 km and can approach and even exceed 3 km. However, the local closure schemes consistently underpredict the boundary layer depth, often by a factor of 2. Comparisons against observed soundings indicate that the differences between the boundary layer depth from the local

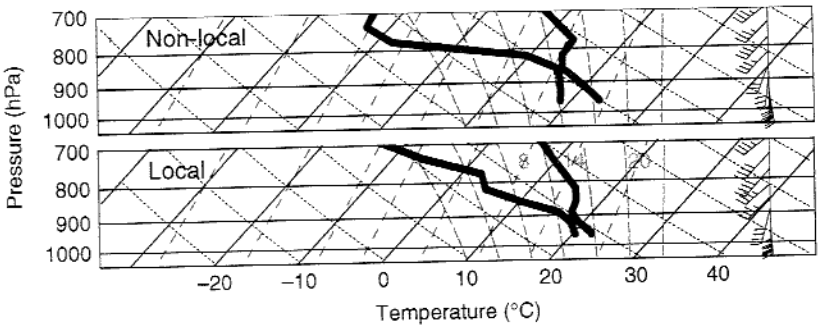

Figure 5.23. Model forecast soundings from 0000 UTC 4 May 1999 using (top) a non-local closure scheme and (bottom) a local closure scheme. Note the differences in boundary layer depth and moisture from the two schemes, as well as the strength of the capping inversion. The lowest model level winds also are different, with the non-local scheme developing an easterly component to the wind not seen in the scheme with the local closure scheme. After Stensrud and Weiss (2002).

closure schemes and observations are significant at the 5% level, indicating that the local closure schemes consistently produce boundary layers that are too shallow over Arizona. Differences between the boundary layer depth from non-local schemes and observations are not significant, indicating that these schemes typically produce reasonable boundary layer structures. Errors in the boundary layer structure also influence the amount of convective available potential energy (CAPE) present in the atmosphere, with the local closure schemes overestimating CAPE by a factor of 2 on average (Bright and Mullen 2002). This result emphasizes the connections between the boundary layer evolution and the potential for deep convection.

Unfortunately, these differences in boundary layer structure from local and non-local closure schemes are not limited to Arizona in the summertime. Results from a mesoscale model forecast of the 3 May 1999 tornado outbreak over Oklahoma also reveal distinct differences between the boundary layers produced by local and non-local closure schemes (Fig. 5.23). The boundary layer depth, structure, and wind profile produced by the non-local scheme compares better with observations than does the local scheme (Stensrud and Weiss 2002). However, there also are occasions when a local closure scheme provides a better forecast than a non-local closure scheme (Deng and Stauffer 2006). Selecting which type of scheme will produce the best forecast for a given location in advance is not easy.

While the difference in boundary layer structure from local and non-local closure is often noticed at observation times, these structures differ throughout the model forecasts (Fig. 5.24). Similar differences are seen in Alpaty *et al.*

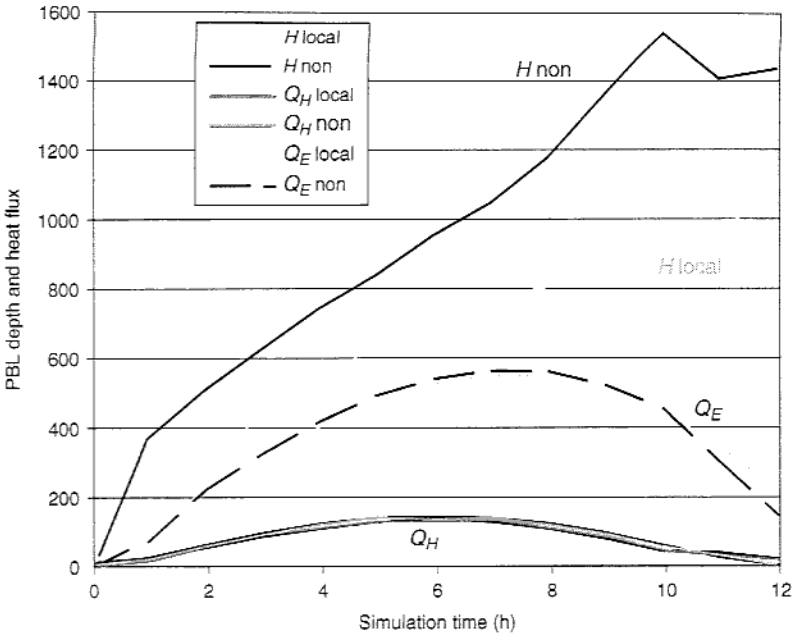

Figure 5.24. Boundary layer height H (m), sensible heat flux Q_H (W m^{-2}) and latent heat flux Q_E (W m^{-2}) for grid point in southeastern South Dakota from simulation starting 1200 UTC 28 June 1997. Model initial conditions and parameterizations are identical, except for the boundary layer. Either a non-local (non) or local scheme is used. While the surface fluxes generally are within 20 W m^{-2} throughout the first 10 h of simulation time, the differences in boundary layer depth are large with the local scheme always producing a shallower boundary layer than the non-local scheme for this case.

(1997) who compared four different boundary layer schemes with observations from both Wangara and FIFE. Since boundary layer schemes influence the wind profiles, not only the potential for deep convection, but the type of deep convection that may be expected to develop (e.g., a multi-cell versus a supercell thunderstorm) is influenced by the boundary layer scheme.

The performance of five boundary layer schemes in the prediction of the diurnal cycles of surface temperature and wind speed is evaluated by Zhang and Zheng (2004), who find that while the diurnal cycle of surface temperature is predicted well by all schemes there are large differences in the diurnal cycle of surface wind speed. In general, all five schemes underestimate the surface wind speed during the daytime and several of the schemes overestimate the surface wind speed at night. Again, the feedbacks between parameterization schemes are widespread and are often difficult to understand for a given forecast situation a priori.

As model grid spacing decreases to the point where the horizontal grid spacing approaches the vertical depth of the boundary layer, then some of

the largest thermals can be resolved explicitly to some extent by the model. Large-eddy simulations that explicitly represent turbulent processes associated with the larger eddies in the boundary layer often use horizontal grid spacings of 100 m or less (Agee and Gluhovsky 1999), yet still may have problems representing some physical processes (Stevens *et al.* 2005). Thus, horizontal grid spacings of 1–2 km are far from that needed to explicitly resolve turbulence, but are small enough that the model likely develops some overturning circulations in the boundary layer. One challenge to boundary layer parameterization schemes as horizontal grid spacing decreases is how to distinguish the mixing explicitly created by the model from the mixing that still needs to be parameterized on the subgrid scale. In addition, at smaller grid spacings horizontal gradients of wind shear also may be important to the generation of turbulence and these effects are not included in any of the boundary layer schemes discussed previously.

One could go further, however, in outlining the concerns regarding all boundary layer parameterizations, for both local and non-local closure approaches. From the perspective of a model user, it seems apparent that most boundary layer schemes have been thoroughly tested against only a handful of data sets. Most of these data sets are from detailed boundary layer observational studies that focused on areas of relatively flat and well-behaved terrain regions with consistent vegetation. While these locales offered good test grounds for examining boundary layer evolution in the best of circumstances, the surface of the Earth is often far from these conditions. Mountains, streams, rolling hills, and vegetation patchiness abound! When observations are taken in regions near complex terrain, the resulting behavior of the boundary layer does not always correspond well with our expectations. Schneider and Lilly (1999) indicate that a number of common simplifying parameterizations are not appropriate for the boundary layer behavior they observed (Fig. 5.25). In addition, boundary layer roll circulations can develop in clear air and influence boundary layer development. The effects of these rolls are not included in most boundary layer schemes.

Few boundary layer schemes have been rigorously evaluated in complex terrain or under highly variable surface conditions, so what we are doing is applying schemes that have been tuned to a handful of data sets (often in pristine surface and environmental conditions) to all conditions across the globe. Amazingly, the success of this application can be seen daily in the consistent utility of numerical model weather forecasts, suggesting strongly that some of the signals must be correct. But this does not mean that these forecasts of boundary layer development should be expected to be correct, or nearly correct, in all circumstances. The boundary layer certainly is not

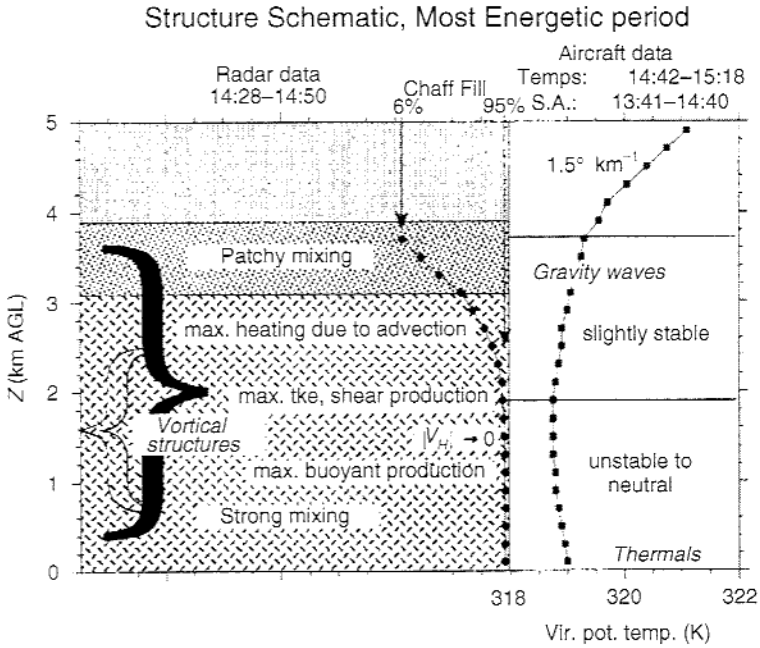

Figure 5.25. A structure schematic of the daytime boundary layer characteristics observed near Boulder, Colorado, during the Phoenix II experiment. Strong mixing occurs near the ground surface, with vortical structures in the middle of the boundary layer, and patchy mixing from gravity waves and shear turbulence production near the top of the boundary layer. From Schneider and Lilly (1999).

observed everywhere, nor do we really know what to expect regarding boundary layer evolution over some regions. There is no guarantee that the predictions from boundary layer schemes will always be successful. Furthermore, none of the schemes summarized previously allows for the direct influence of clouds on boundary layer development, except when saturation occurs on the grid scale. Instead, shallow convective parameterizations and cloud cover parameterizations have been developed to account for the effects of clouds within boundary layers (see Chapters 6 and 9). As this discussion suggests, there are many unsolved issues surrounding boundary layer parameterization that deserve attention.

5.8 Questions

1. Following the outline provided by the section on Reynolds averaging and turbulence closure, derive the equations for the perturbation velocity and potential temperature

$$\frac{\partial u_i'}{\partial t} = \cdots$$

$$\frac{\partial \theta'}{\partial t} = \cdots$$

the equations for the turbulent fluxes

$$\frac{\partial(\overline{u_i' u_j'})}{\partial t} = \cdots$$

$$\frac{\partial(\overline{u_i' \theta'})}{\partial t} = \cdots$$

and the equations for the variances

$$\frac{\partial \overline{u_i'^2}}{\partial t} = \cdots$$

$$\frac{\partial \overline{\theta'^2}}{\partial t} = \cdots$$

Begin by expanding the variables into a mean and a perturbation component and use the Boussinesq equation (5.3) and

$$\frac{\partial \theta}{\partial t} + u_j \frac{\partial \theta}{\partial x_j} = \nu \frac{\partial^2 \theta}{\partial x_j^2}.$$

Show all work.

2. Using knowledge of turbulence closure, discuss the pros and cons to going to higher-order closure schemes (i.e., third-order closure).
3. One set of equations for a mixed layer model is

$$\frac{d\overline{\theta}}{dt} = \frac{(1 + k_e) C_T V_S (\theta_S - \overline{\theta})}{H},$$

$$\frac{dH}{dt} = k_e C_T V_S \frac{(\theta_S - \overline{\theta})}{\Delta\theta},$$

$$\frac{d\overline{q}}{dt} = C_T V_S \frac{M(q_S - \overline{q}) + [k_e(\theta_S - \overline{\theta})\Delta q/\Delta\theta]}{H},$$

where M denotes the moisture availability, C_T is a transfer coefficient, and V_S is the surface wind speed. Let us now examine the consequences of changing both the entrainment parameter k_e and the moisture availability. Assume the following: $C_T = 0.015$; $V_S = 10\,\mathrm{m\,s^{-1}}$; $M = 0.5$; $\theta_S = 311\,\mathrm{K} + 10\Delta t\,(3\,\mathrm{h})^{-1}$ (the potential temperature increases linearly with time to 321 K at 3 hours and 331 K at 6 hours); and $q_S = 17\,\mathrm{g\,kg^{-1}} - 2.5\Delta t\,(3\text{ hours})^{-1}$ (the mixing ratio decreases by $2.5\,\mathrm{g\,kg^{-1}}$ over 3 hours). Also assume that the initial environmental potential temperature and mixing ratio profiles look like

$\theta = 310\,\mathrm{K} + 5\,\mathrm{K} \times z\,(1000\,\mathrm{m})^{-1}$
$q = 11\,\mathrm{g\,kg^{-1}}$ at and below $z = 1000\,\mathrm{m}$
$q = 3\,\mathrm{g\,kg^{-1}}$ above $z = 1000\,\mathrm{m}$,

where $H = 30\,\mathrm{m}$ at time zero (if H is zero at time zero, then the model blows up). Develop a finite-difference version of these mixed layer equations and integrate the equations for 3 and 6 hours using three different values of k_e: 0.1, 0.3, and 0.5. Then answer the following questions. What are the final values of θ and q in the mixed layer? What are the final values of the mixed layer depth H? What do these results say about the importance of choosing an appropriate value for the entrainment coefficient when using a PBL model? Do these differences increase or decrease over longer time periods?

One simple integration scheme is to define $x'_{i,n} = f(x_{i,n})$, where i denotes the variable ($i = 1, 2, 3$) and n is the time level, and then integrate forward one time step to $n+1$ using $x_{i,n+1} = 0.5\left[x_{i,n} + \tilde{x}_{i,n+2}\right]$, where one first determines $\tilde{x}_{i,n+1} = x_{i,n} + f(x_{i,n}) \times \Delta t$ and then determines $\tilde{x}_{i,n+2} = \tilde{x}_{i,n+1} + f(\tilde{x}_{i,n+1}) \times \Delta t$. This simple time integration scheme is stable for the mixed layer model, but requires a time step of about 1 s.

4. Using the program developed in Question 3, assume that the land surface scheme has a bias of $+1\,\mathrm{K}$ in the temperature forecast over a 3 h period. Thus, $\theta_S = 311\,\mathrm{K} + 11\Delta t\,/\,(3\text{ hours})$. Rerun the mixed layer scheme with this surface temperature evolution and with $k_e = 0.3$. What are the values of the mixed layer depth H at 3 and 6 hours? How do these changes compare with changes in the entrainment coefficient?
5. Using the same initial potential temperature and mixing ratio profiles as in Question 3, and with the same time rate of change of the surface potential temperature and the mixing ratio, develop a simple finite-difference model of the lowest 10 000 m of the atmosphere based only upon K-theory mixing. Use

$$\frac{\partial \bar{\theta}(z)}{\partial t} = K_H \frac{\partial^2 \bar{\theta}(z)}{\partial z^2}$$

and

$$\frac{\partial \bar{q}(z)}{\partial t} = K_H \frac{\partial^2 \bar{q}(z)}{\partial z^2},$$

and set up a vertical grid starting at the surface ($z = 0$ so that $\theta_s = \bar{\theta}(0)$) with 50 m vertical increments. Here $\bar{\theta}$ is the mean potential temperature of a given layer and it is allowed to vary with height. Assume that K_H is a constant. The time evolution of potential temperature and the mixing ratio at $z = 0$ is then specified. Try the finite-difference approximation

$$F_{m,n+1} = F_{m,n} + \frac{K_H \Delta t}{(\Delta x)^2}\left(F_{m+1,n} + F_{m-1,n} - 2F_{m,n}\right),$$

where m is the vertical grid level and n is the time level. Try time steps of 1 s. Integrate the model out to 6 h and examine the potential temperature and mixing

ratio profiles. Try using several values of K_H between 10 and 200. What behaviors are seen? Is this result realistic?

6. Obtain an observed sounding from near local noon or late afternoon (00:00 UTC in the USA is fine) and a corresponding 2 m temperature and mixing ratio. Determine the positive and negative areas of this sounding, as defined from the penetrative convection non-local closure scheme, and the boundary layer top. Using the diffusion scheme, calculate the surface value of $\theta_v + \theta_T$ and from this value also the boundary layer top. Finally, using the observed wind and thermodynamic profiles, estimate values for K_H within this boundary layer using mixing-length theory as in (5.59) and (5.61). How does the implied mixing from the local closure scheme compare to the implied mixing from the non-local closure schemes? Explain.
7. Choose a single observed sounding location site and compare the observed soundings against model forecast soundings at all available observation times for a 7 day period. Construct a table comparing the boundary layer depth, the mean boundary layer potential temperature, and the mean boundary layer mixing ratio from both the model and the observational data. Separate the data based upon the observation time. Summarize the results.